

Dynamics of gas-liquid annular flow: from wall-film instability to fragmentation

Yoshiaki Kamada, Zhenying Wang^{1,2} and Chihiro Inoue o

Corresponding author: Chihiro Inoue, inoue.chihiro@aero.kyushu-u.ac.jp

(Received 10 June 2025; revised 22 October 2025; accepted 22 October 2025)

We highlight the complete transition from liquid-wall-film instability of an annular gasliquid flow inside a nozzle to spray formation at the trailing edge, aiming to identify two distinct flow regimes of ripple waves and disturbance waves and to clarify their distinct fragmentation mechanisms. Experiments conducted under strictly controlled boundary conditions support our theoretical analysis, revealing that the onset of disturbance waves coincides with the liquid-film Weber number (We) of unity, marking a significant change in following fragmentation dynamics. For We < 0.5, the liquid wall film forms three-dimensional ripple waves driven by the superposition of Kelvin-Helmholtz and Rayleigh-Taylor (RT) instabilities, with no disturbance waves present. At the trailing edge, the liquid film temporarily accumulates, extends into isolated ligaments along the axial direction via RT instability, and subsequently fragments into droplets through Plateau–Rayleigh instability, displaying a weak coupling between ripple wave dynamics and fragmentation. In contrast, for We > 0.5, disturbance waves with long wavelengths and large amplitudes become prominent, superimposed on the base ripple waves. As these disturbance waves reach the trailing edge, they are spontaneously ejected as liquid sheets at the same frequency, forming transverse rims through RT instability and rapidly disintegrating into fine droplets. This regime demonstrates a direct coupling between disturbance-wave dynamics and fragmentation.

Key words: aerosols/atomization, breakup/coalescence, drops

¹Department of Aeronautics and Astronautics, Kyushu University, 744 Motooka, Nishi-Ku, Fukuoka 819-0395, Japan

²International Institute for Carbon-Neutral Energy Research (WPI-I²CNER), Kyushu University, 744 Motooka, Nishi-Ku, Fukuoka 819-0395, Japan

1. Introduction

Liquid wall films interacting with turbulent gas flows exhibit a variety of complex interfacial phenomena, ranging from wave formation, ligament elongation to fragmentation into droplets. These processes are commonly encountered in industrial applications such as heat exchangers, gas turbines, nuclear reactors, distillation columns, etc. Understanding the sequence of these phenomena is critical for accurately predicting interfacial mass, momentum and heat transfer in those practical situations. Despite decades of experimental, theoretical and numerical research, gas-liquid flows remain challenging to analyse due to their inherently multiscale and multiphysics characteristics, and the underlying fluid-dynamic mechanisms are still not fully understood (Azzopardi 1997; Ishii & Hibiki 2010; Xue et al. 2022). Liquid films can rapidly evolve from millimetre-scale wave structures to micron-scale droplets. Capturing the full dynamic range of these transformations requires further experiments and simulations with ultrahigh spatio-temporal resolution. Comprehensive investigations that link internal nozzle-flow characteristics to the resulting droplet formation are essential for a wide range of practical applications, such as fuel nozzles in aircraft engines and film dynamics in steam boilers. Continued advancements in both measurement techniques and modelling approaches are essential to address these issues and enable a more comprehensive understanding of gas-liquid interfacial dynamics.

As a representative form of nozzle and pipe flow, gas-liquid annular flow has been extensively investigated. A foundational contribution to this field is the classification of a wide range of flow regimes by Hewitt & Roberts (1969), which continues to be widely cited. Taylor & Hewitt (1963) identified two principal types of instability waves in annular flows: high-frequency, small-amplitude ripple waves and low-frequency, large-amplitude disturbance waves. Various dimensionless numbers, such as the Weber, Ohnesorge and Reynolds numbers, have been employed to characterise the onset of disturbance waves (Hutchinson & Whalley 1973; Ishii & Grolmes 1975; Andreussi, Asali & Hanratty 1985; Crowe 2005).

Subjected to shear flow, the liquid film, as well as the jet interface, initially develops axial waves due to the Kelvin-Helmholtz (KH) instability, which arises from the velocity difference between the gas and liquid phases. Subsequently, transverse perturbations are generated by the Rayleigh-Taylor (RT) instability driven by the density difference between the two phases. The interaction and superposition of these axial and transverse instabilities lead to the formation of three-dimensional wave structures on the liquid surface, resulting in ripple waves. From the crests of these waves, thin ligaments extend outward and eventually break up into droplets through the Plateau-Rayleigh (PR) instability (Marmottant & Villermaux 2004). The liquid-film characteristics of flat-plate and pipe flows can be unified through an interfacial friction coefficient (Inoue & Maeda 2021). Inoue et al. (2022) successfully predicted the dryout point of the liquid film under high-temperature gas flow by considering the effects of entrainment and the increase in surface area due to wave formation. Recent advances in numerical modelling have further enabled the prediction of complex interfacial structures, such as vortices and wave characteristics on the liquid-film surface, which are otherwise difficult to observe directly (Zandian, Sirignano & Hussain 2018). Jiang & Ling (2021) employed direct numerical simulation (DNS) to investigate how turbulence intensity influences unstable waves in both the streamwise and transverse directions. They visualised the expansion of holes on the wave surface, the subsequent formation of Taylor-Culick rims at their edges, and their eventual break up into droplets.

The ripple waves tend to merge downstream, resulting in a decrease in wave frequency and the formation of coherent azimuthal structures of disturbance waves (Zhao et al. 2013;

Isaenkov et al. 2019). These disturbance waves are closely related to the onset of droplet entrainment, which is important for accurately predicting the interfacial friction coefficient at the gas-liquid interface. Liquid-film thickness, a key parameter in characterising disturbance waves, has been measured using various techniques, leading to numerous empirical correlations (Berna et al. 2014). The crests of disturbance waves can rise several times higher than the base film and are further accelerated by aerodynamic forces. Moreover, the wave front frequently deforms into a horseshoe shape, which promotes frequent droplet entrainment (Cherdantsev 2023). Taylor & Hewitt (1963) measured the frequency of the waves and suggested that disturbance waves contribute to the transport of the liquid film. Le Corre (2022) developed a phenomenological model for annular film flow, treating disturbance waves as an additional wave field superimposed on the base liquid film. Their approach accounts for non-equilibrium effects during film development and improves the accuracy of predicting key flow parameters. Cherdantsev, Isaenkov & Markovich (2025) proposed that both local perturbations and a sufficient liquid flow rate exceeding the viscous layer are necessary for the formation of disturbance waves. Zhang et al. (2023) reported that disturbance waves on wing surfaces affect ligament formation at the trailing edge.

The free liquid jet discharged from a nozzle is atomised into fine droplets by high-speed airflow. Marmottant & Villermaux (2004) established a comprehensive model that describes the instability mechanisms in coaxial jets, leading to predictions of droplet sizes and their distribution. The liquid jet first becomes unstable due to shear instability, whose wavelength is proportional to the characteristic wavelength of KH instability (Varga, Lasheras & Hopfinger 2003; Singh *et al.* 2020). As the liquid film grows perpendicular to the airflow, it is subjected to acceleration by aerodynamic forces. Subsequently, RT instability induces transverse undulations, leading to the formation of ligaments and following bag structures, which ultimately govern the final droplet size (Varga *et al.* 2003; Marmottant & Villermaux 2004; Chaussonnet *et al.* 2016; Choi, Byun & Park 2022; Oshima & Sou 2024). Matas, Delon & Cartellier (2018) conducted a linear stability analysis of the destabilisation process in a liquid jet and derived scaling laws for the wave frequency. These predictions were validated through both experimental and numerical investigations by Singh *et al.* (2020) and Bozonnet *et al.* (2022).

Several scenarios have also been proposed for liquid-sheet atomisation. Liquid sheets fragment through the formation of holes caused by local variations in thickness and velocity (Dombrowski & Fraser 1954; Villermaux 2020). Lhuissier & Villermaux (2013) investigated the full sequence of hole expansion and ligament breakup in thin liquid films. As holes expand, the volume of the liquid film becomes concentrated in the ligaments, and the break up of a single ligament contributes to variability in droplet sizes within the overall spray. Néel et al. (2020) proposed a theoretical threshold for sheet-like lamella formation resulting from collisions at the edges of holes in thin liquid films. Lamellae are deformed into ligaments due to RT instability, and their diameter scales with their thickness. When a liquid film is exposed to intense aerodynamic forces such as cross-flow, it fragments into bags and ligaments. The bag structure is characterised by an extremely thin liquid membrane of the order of micrometres. The collapse of the perforated sheet follows the Taylor-Culick law, and the resulting droplet size from bag breakup is almost independent of air velocity (Ng, Sankarakrishnan & Sallam 2008; Oshima & Sou 2024; Varkevisser et al. 2024). Oshima & Sou (2024) developed a phenomenological model that predicts droplet sizes resulting from ligament and bag breakup, based on observations of a planar liquid film subjected to co-current airflow.

Following the primary atomization of a liquid sheet, finer droplets are formed under significant aerodynamic forces (secondary atomization). When the Weber number of

these droplets exceeds approximately 10, secondary atomization with bag breakup occurs, causing the droplets to disintegrate into finer scales (Guildenbecher, López-Rivera & Sojka 2009). In the bag-breakup regime, a droplet undergoes deformation, forming a thin, membrane-like structure bordered by a thicker toroidal rim. Under the influence of aerodynamic forces, the central bag inflates and eventually ruptures, while the rim forms several nodes and fragments into smaller droplets (Jackiw & Ashgriz 2022; Kulkarni *et al.* 2023).

There is ongoing debate regarding the most appropriate probability distribution to describe droplet sizes produced by spray fragmentation. Previous studies have reported various forms, including single-parameter gamma distributions (Marmottant & Villermaux 2004; Villermaux 2007), compound gamma distributions (Kooij *et al.* 2018; Jackiw & Ashgriz 2022) and log–normal distributions (Jackiw & Ashgriz 2023). These models differ in their underlying assumptions, such as ligament corrugation, the width of the ligament size distribution and the presence of multiple fragmentation modes.

Previous studies have made significant progress in elucidating individual mechanisms such as interfacial instabilities on liquid wall films and the fragmentation of free jets and sheets, while a unified theoretical framework that links upstream wall-film dynamics to downstream droplet fragmentation is still lacking. In particular, the criteria for distinguishing flow regimes of ripple waves and disturbance waves, as well as the corresponding fragmentation mechanisms at the trailing edge, remain unclear. For quantitative predictions of the statistics of spreading droplets, it is essential to understand the complete scenario of liquid-wall-film dynamics to the fragmentation. Therefore, in this study, we conduct a comprehensive investigation of gas—liquid annular flow, spanning from wall-film instabilities to final droplet formation. Based on detailed measurements and scaling analysis, we develop a theoretical model that captures the entire sequence of wall-film dynamics, ligament formation and fragmentation. Although the present study employs an annular pipe configuration, the underlying interfacial dynamics is also relevant to a planar flow on a plate.

The following context is structured as follows: § 2 describes the experimental set-up and conditions that establish well-defined boundary conditions for the liquid and gas flows; § 3 presents the experimental results for two distinct flow regimes and discusses the underlying physical mechanisms based on scaling laws; and § 4 summarises the key findings of this study.

2. Experimental set-up

Many previous experiments on liquid wall films, including subsequent spray formation, examined liquid films in a rectangular channel (Andreussi *et al.* 1985; Shinan *et al.* 2019) or on a wing (Inamura *et al.* 2019; Zhang *et al.* 2023). In these situations, a major challenge is to fix the gas-side velocity-boundary-layer thickness due to changes in the cross-sectional flow area and sidewall effects. For the liquid flow, it is generally difficult to achieve a liquid film with uniform thickness in the transverse direction under any gas-side velocity. To overcome these practical challenges, we establish an annular flow system with airflow in the centre and a liquid film along the pipe wall, allowing for well-controlled boundary conditions for both gas and liquid phases (Kamada *et al.* 2025a). When the pipe diameter is sufficiently large compared with the film thickness, the effect of pipe curvature is negligible as it is equivalent to a planar flow.

Figure 1(a) illustrates a schematic diagram of the experimental set-up. Air pressurised by a screw compressor (GP37BSD-D, IHI) is stored in a tank with a maximum pressure of 0.7 MPa. The total pressure of the airflow is controlled using a precision regulator (IR3000,

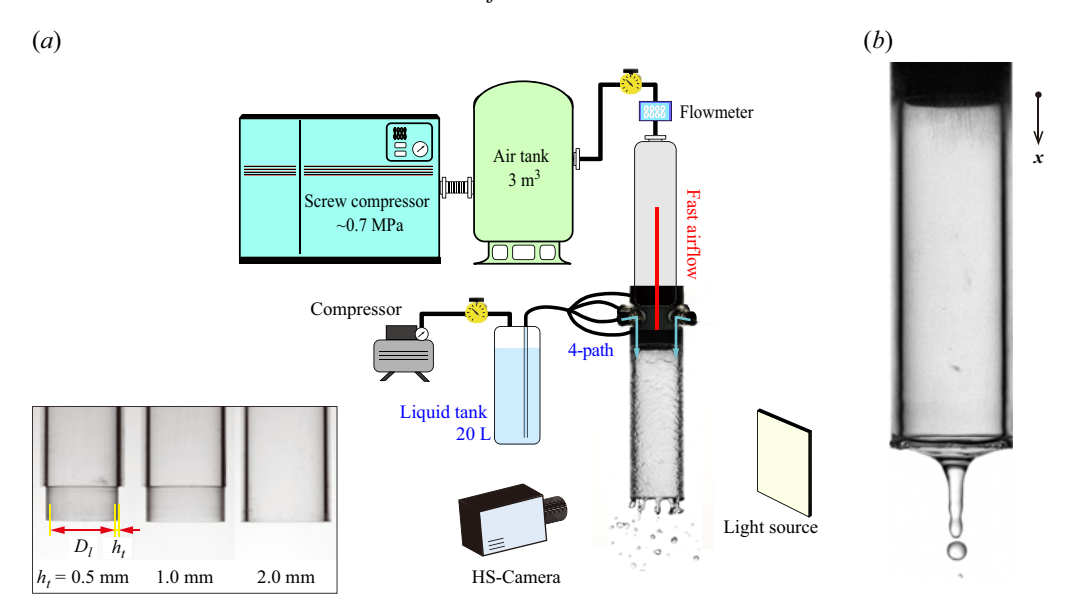


Figure 1. (a) Schematic diagram of the experimental set-up. (b) Liquid-film flow at mean gas velocity $u_g = 0 \text{ m s}^{-1}$. The x-axis is defined in the axial direction with the gas exit as the origin.

SMC), and the airflow rate is monitored using a thermal mass flowmeter (TF1050, OVAL). Through a long stainless steel pipe with an inner diameter of $D_g = 19$ mm and a length of 500 mm, the airflow becomes a fully developed turbulent flow forming velocity profile of the 1/7-power law (see Appendix A). Then, the airflow goes through the centre of an acrylic pipe with an inner diameter of $D_l = 21$ mm. The axial length of the transparent test section is 100 mm. The working fluid of water is supplied from a pressurised tank. It flows through four branched tubes spaced at 90° intervals and enters the gap between the stainless steel pipe and the acrylic pipe, corresponding to an initial liquid-film thickness of h = 0.5 mm. The flow rate of the liquid film is calculated by measuring the weight of water collected in a certain period before the experiment, with a relative error of ± 0.5 %. Since the amount of liquid accumulated on the exit plane of the pipe affects the subsequent fragmentation process, we use different trailing-edge thicknesses h_t of 0.5, 1.0 and 2.0 mm. Figure 1(b) shows the visualisation results when only the liquid film flows through the test section without central airflow. The smooth liquid film flowing along the inner wall concentrates at the centre of the pipe end and elongates into a single ligament, from which droplets break up. This observation confirms that the present experimental set-up successfully produces a liquid wall film with uniform thickness along the circumferential direction.

Table 1 summarises the experimental conditions. The mean gas velocity reaches up to 100 m s⁻¹. We define the gas Reynolds number as $Re_g = \rho_g u_g D_l/\mu_g$ and the liquid-film Reynolds number as $Re_l = \rho_l u_m h/\mu_l = Q_l/(\pi D_l v_l)$, where u_m is the mean film velocity and Q_l is the volume flow rate of the liquid. At a room temperature of 25 °C, the liquid density is $\rho_l = 997$ kg m⁻³, dynamic viscosity is $\mu_l = 0.89 \times 10^{-3}$ Pa s, kinematic viscosity is $\nu_l = 0.89 \times 10^{-6}$ m² s⁻¹, the gas density is $\rho_g = 1.18$ kg m⁻³, and dynamic viscosity is $\mu_g = 1.82 \times 10^{-5}$ Pa s. The surface tension coefficient of water is $\sigma = 0.072$ N m⁻¹.

We visualise a series of annular pipe flows and the subsequent fragmentation process using a high-speed camera (Fastcam Mini AX-100, Photron) at frame rates of up to

Mean gas velocity, u_g $10 \sim 100 \, \mathrm{m \, s^{-1}}$ Gas Reynolds number, Re_g $1.4 \times 10^4 \sim 1.4 \times 10^5$ Mean film velocity, u_m $0.14 \sim 1.6 \, \mathrm{m \, s^{-1}}$ Liquid-film Reynolds number, Re_l $30 \sim 200$

Table 1. Experimental conditions.

 $10\ 000\ f.p.s.$, and measure the properties of waves, ligaments and droplets using ImageJ software (Schneider, Rasband & Eliceiri 2012). For the measurement of droplet diameter, we use a pulsed light source (Cavilux Smart UHS, Cavitar) synchronised with the camera. Exposure time of the light is set to 20 ns to eliminate motion blur. We visualise spherical droplets at 200 mm away from the pipe exit with a spatial resolution of $10\ \mu m/pixel$ and at a recording rate of $100\ f.p.s.$ to avoid double-counting the same droplet. For each experimental condition, more than $10\ 000$ in-focus droplets are analysed to obtain statistically converged size distributions. The analysis method is described in Appendix B.

3. Results and discussion

First, we identify the two flow patterns of annular flow as the ripple-wave regime and the disturbance-wave regime. Then, for each flow regime, we perform detailed measurements and modelling of all intermediate steps from interfacial instabilities developed inside the pipe to droplet statistics after ejection from the pipe end.

3.1. Film-flow pattern and the criterion

Taylor & Hewitt (1963) categorised the waviness of annular flow into (i) ripple waves alone and (ii) ripple waves accompanied by larger-scale disturbance waves. We here denote these as the ripple-wave regime and the disturbance-wave regime, respectively. Visualisation results for each regime are shown in figure 2 as well as in the supplementary movie 1 available at https://doi.org/10.1017/jfm.2025.10869. In the ripple-wave regime in figure 2(a), the surface is covered with scaly waves. At the downstream end of the pipe, cylindrical ligaments elongate and break up into droplets. As Re_g and/or Re_l increase, a coherent structure of disturbance waves becomes visible at x = 50 mm in figure 2(b). The phase velocity of disturbance waves exceeds that of ripple waves, and droplet entrainment is frequently observed from the wave crests. Upon reaching the pipe end, the ejected sheet flutters and disintegrates into fine droplets smaller than 300 μ m in diameter. Figure 2(c,d) show spatio-temporal diagrams of the liquid film at $x = 70 \sim 90$ mm. In the ripple-wave regime in figure 2(c), the waves propagate orderly at a constant velocity. In the disturbancewave regime in figure 2(d), wave-merging events are observed, wherein long disturbance waves overtake and converge with preceding ripple waves. Since the lines in the spatiotemporal diagram are nearly straight, the disturbance waves as well as the ripple waves propagate at a constant phase velocity, reaching a quasi-steady state within the test section.

Figure 3(a) shows the flow regime transitions from the ripple-wave regime to the disturbance-wave regime as u_g increases under a constant Re_l . Accordingly, the breakup pattern at the pipe exit changes from isolated ligaments to a corrugated sheet. Based on flow visualisations over a wide range of flow conditions, the two regimes can be distinguished in the regime map presented in figure 3(b), which shows that the onset of disturbance waves depends on both Re_g and Re_l , consistent with past experimental results by Andreussi *et al.* (1985). To theoretically identify the threshold distinguishing the two

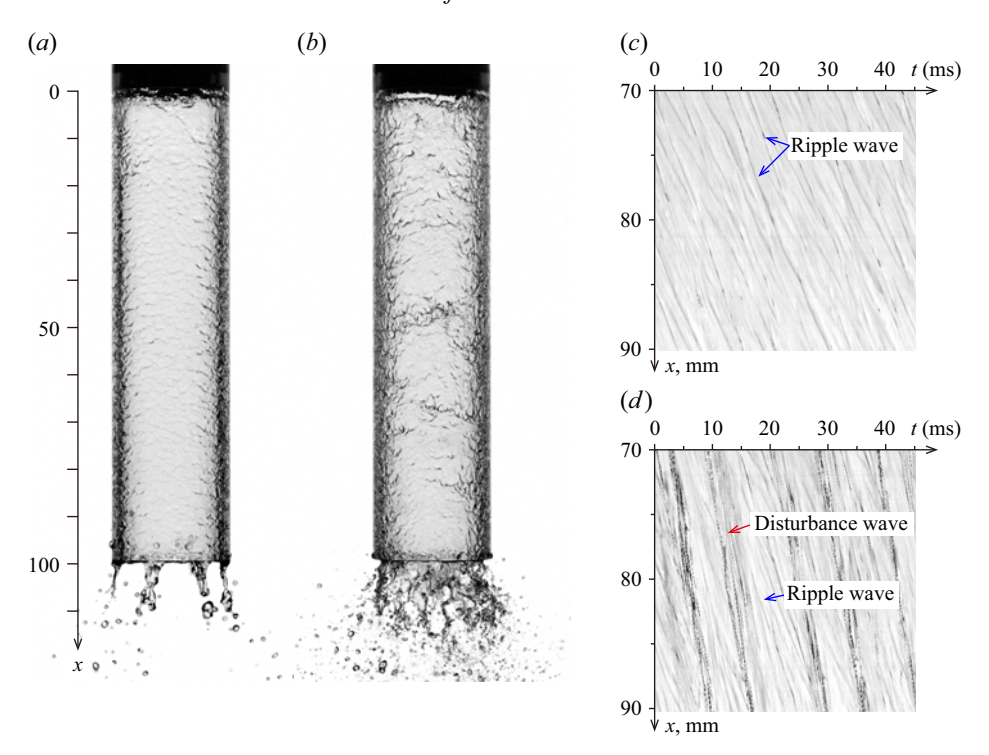


Figure 2. (a,b) Visualisation results. (c,d) Spatio-temporal diagram of the liquid film in 70 mm $\le x \le 90$ mm. The dark lines indicate the wave fronts, and their inclination corresponds to the wave velocity. (a,c) Ripple-wave regime $(Re_l = 30, Re_g = 8.4 \times 10^4)$. (b,d) Disturbance-wave regime $(Re_l = 160, Re_g = 8.4 \times 10^4)$.

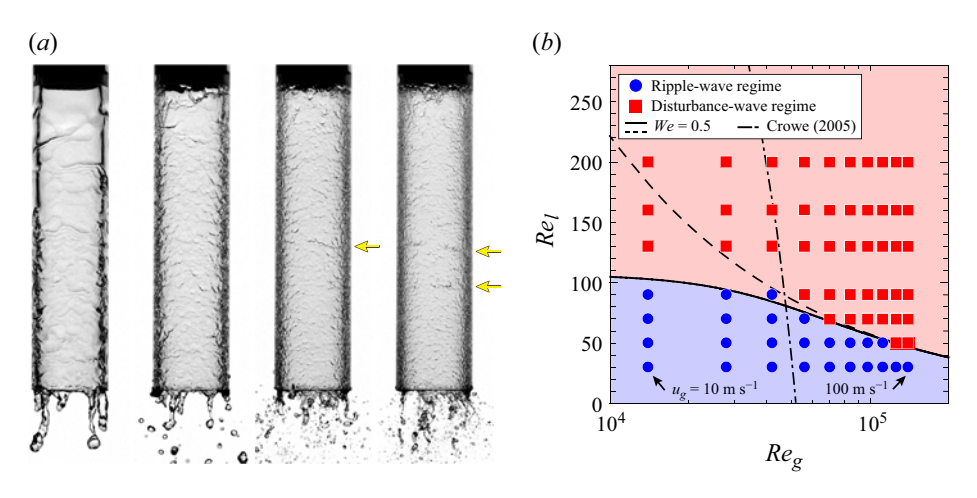


Figure 3. (a) Visualisation results at $Re_l = 70$. From left to right: $u_g = 20$, 40, 60 and 80 m s⁻¹. The yellow arrows indicate the disturbance waves. (b) Flow-regime map for gas and liquid-film Reynolds numbers. The solid line presents We = 0.5, considering both gravity and airflow shear by (3.2), while the dashed line takes into account only airflow shear by (3.3). The dash-dotted line represents the capillary-length model of Crowe (2005).

regimes, we consider the dominant effects of liquid-film inertia and surface tension at the gas-liquid interface. The vertically falling liquid film is subjected to both shear stress of the airflow and gravity, with viscous stress within the film also being involved. By introducing the friction factor f, the interfacial shear stress τ can be expressed as

$$\tau = \frac{1}{2} f \rho_g u_g^2. \tag{3.1}$$

We adopt the Blasius correlation, $f = 0.08 Re_g^{-1/4}$ (Nikuradse 1933; Moody 1944), which is valid for turbulent flow in smooth pipes up to $Re_g = 10^5$ (see Appendix C). From the two-dimensional steady-state Navier–Stokes equation, the mean liquid-film thickness h is given by Alekseenko & Nakoryakov (1995) as,

$$\frac{gh^3}{3\nu_l} + \frac{\tau h^2}{2\mu_l} = Re_l \nu_l, \tag{3.2}$$

where g is the gravitational acceleration. As u_g increases, the effect of gravity becomes negligible for the film flow, resulting in a Couette flow simply sheared by the airflow. In this case, h is expressed (Inoue & Maeda 2021; Inoue $et\ al.\ 2022$) as

$$\frac{h}{D_l} = \frac{2}{\sqrt{f}} \frac{\mu_l}{\mu_g} \sqrt{\frac{\rho_g}{\rho_l}} Re_l^{1/2} Re_g^{-1}.$$
 (3.3)

Averaged momentum flux of the Couette film flow is $4/3\rho_l u_m^2$, reasonably approximated as $\rho_l u_m^2$. The wave amplitude of a grows to become comparable to h (Shinan et al. 2019). When the inertia ($\approx \rho_l u_m^2$) exceeds the stabilising surface tension at the wave crest ($\approx \sigma/h$), the wave will amplify. Correspondingly, we deduce the onset of disturbance waves by the liquid-film Weber number of the order of unity:

$$We = \frac{\rho_l u_m^2 h}{\sigma} \approx 1. \tag{3.4}$$

By numerically solving (3.2) to obtain h, we calculate u_m based on mass conservation. For instance, we yield $h=83~\mu\mathrm{m}$ and $u_m=0.60~\mathrm{m~s^{-1}}$ at $Re_g=1.0\times10^5$ and $Re_l=50$. Substituting h and u_m into (3.4), we identify a critical Weber number of We=0.5, as denoted by the solid line in figure 3(b), which corresponds well to the experimental results for the onset of disturbance waves. For comparison, the dashed line depicts We=0.5 based on the film thickness of (3.3), which neglects the effect of gravity and follows a similar criterion by Hutchinson & Whalley (1973). While this simplified form agrees with the experiment at high Re_g , it fails to divide the regimes at $Re_g \leq 10^5$, where the Froude number remains small and gravity still influences the film flow. Epstein (1990) proposed a critical Weber number of $\rho_g u_g^2 l_c/\sigma$ based on the capillary length $l_c = \sqrt{\sigma/(g\rho_l)}$, which was later refined by Crowe (2005). However, this criterion shows a discrepancy with the present experimental results.

Figure 4(a) presents the measured wave frequency and phase velocity for 100 waves along the axial direction in the disturbance-wave regime at $Re_l = 130$ and $Re_g = 1.1 \times 10^5$. We define that the subscripts r and d refer to ripple waves and disturbance waves, respectively. For the slow and frequent ripple waves, both the frequency f_r and the phase velocity u_r become constant at $x \ge 30$ mm. At $x \ge 50$ mm, the fast disturbance waves are fully developed, with constant values of f_d and u_d . A similar axial length was required for the developed disturbance waves as confirmed by Isaenkov *et al.* (2019). The constancy of the wave properties confirms that the bulk airflow conditions remain stable within the test section. Figure 4(b) shows histograms of u_r and axial wavelength λ at x = 70 mm obtained

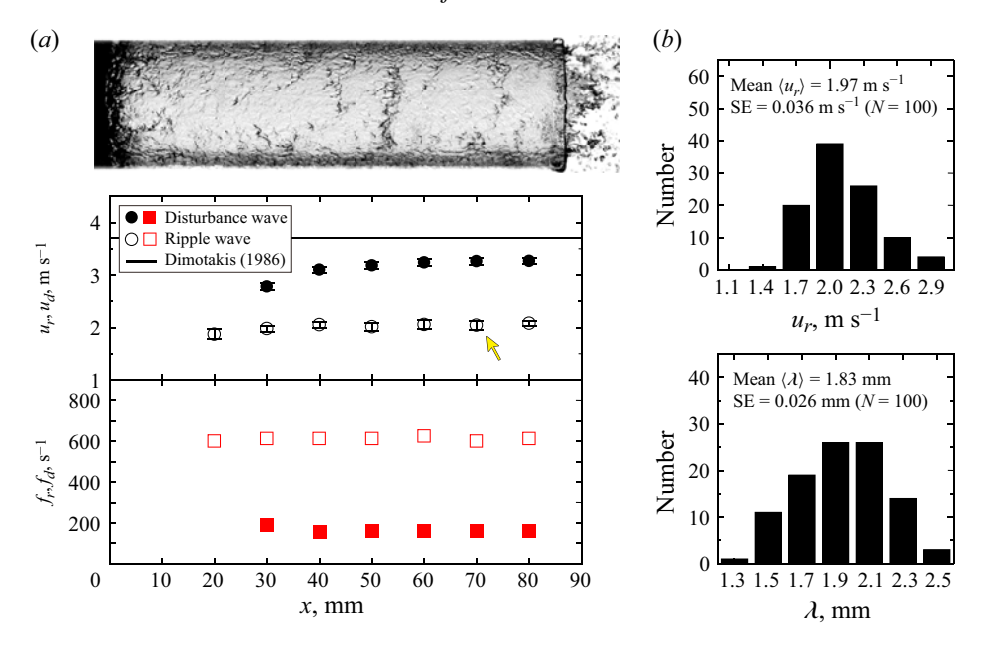


Figure 4. (a) Frequency and phase velocity of disturbance and ripple waves depending on axial position at $Re_l = 130$ and $Re_g = 1.1 \times 10^5$. The red symbols present frequencies, and the black symbols show phase velocities. The solid line shows the theoretical value of (3.7). Error bars depict standard errors (SE). (b) Histograms of the phase velocity and axial wavelength of ripple waves measured at x = 70 mm (depicted by the arrow in (a)).

by measuring ripple waves with a sample number of N = 100. Although we find the broad dispersion around the mean values of $\langle u_r \rangle$ and $\langle \lambda \rangle$, the small standard errors indicate that the mean values are statistically well converged.

As demonstrated in figures 2 and 3, the liquid-wall-film dynamics and the subsequent fragmentation process change significantly at We = 0.5. In the following sections, we discuss the ripple-wave regime for We < 0.5 and the disturbance-wave regime for We > 0.5. We quantify the converged characteristics of ripple and disturbance waves at $x \ge 50$ mm.

3.2. Ripple-wave regime

At We < 0.5, the film surface is covered with fine ripple waves. Figure 5(a) presents the time series visualisation results. Driven by the central airflow, the liquid wall film develops a regular pattern of surface ripples inside the pipe and forms cylindrical ligaments at the trailing edge. These ligaments break up periodically into droplets at intervals of approximately 10 ms. Reflecting the visualisation results, figure 5(b) schematically illustrates the gas flow with mean velocity u_g and vorticity thickness δ above the wall film. The liquid film flows vertically downward along the wall with velocity u_m and thickness h. Ripple waves are characterised by axial wavelength λ and circumferential wavelength λ_p , propagating at a phase velocity u_r . At the trailing edge, the liquid film accumulates on the edge with a thickness of h_t . Then, the ligaments elongate with a transverse distance of λ_t , forming structures with diameter d_t and length l_t . Eventually, droplets of diameter d_r split from the ligament tips over a time period T.

Under the present condition of $u_g \gg u_m$, the liquid film becomes unstable at first due to KH instability, which involves a characteristic length scale δ , defined as $\delta = 2D_l/(fRe_g)$ (Rayleigh 1880; Schlichting & Gersten 2016). The axial wavelength is

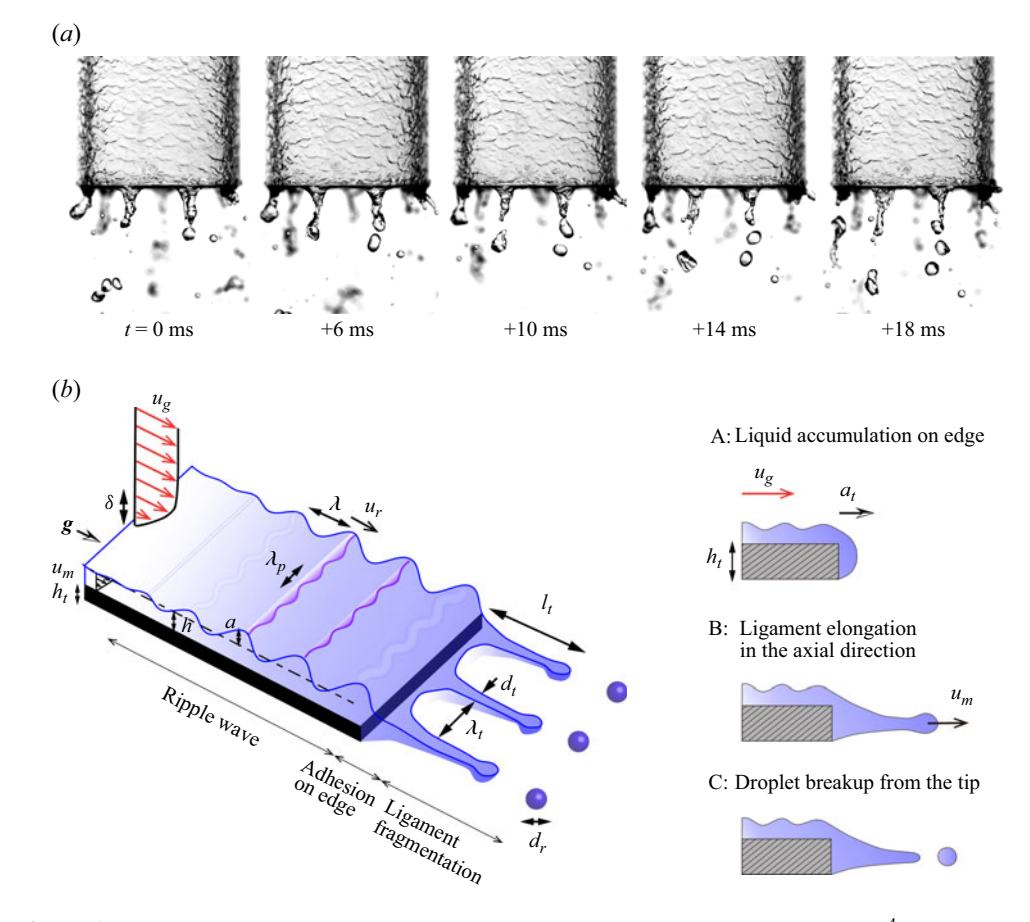


Figure 5. (a) Time series images of ripple wave and ligament breakup at $Re_g = 8.4 \times 10^4$ and $Re_l = 30$. Droplets break up periodically from the tip of the ligament at t = 0, 14 ms. (b) Schematic diagram of film dynamics and fragmentation process in ripple-wave regime.

expressed (Villermaux 1998) independent of capillarity:

$$\lambda \approx \delta \sqrt{\frac{\rho_l}{\rho_g}} = 25 D_l \sqrt{\frac{\rho_l}{\rho_g}} Re_g^{-3/4}.$$
 (3.5)

The shear flow further accelerates the axial waves, leading to RT instability to stimulate circumferential waves (Rayleigh 1882; Taylor 1950). Based on the Weber number with the length scale δ , $We_{\delta} = \rho_g u_g^2 \delta/\sigma$, the circumferential wavelength λ_p is given by Marmottant & Villermaux (2004) as

$$\lambda_p = \delta W e_{\delta}^{-1/3} \left(\frac{\rho_g}{\rho_l}\right)^{-1/3}.$$
 (3.6)

Figure 6(a) shows the experimental results for λ and λ_p of 100 waves inside the pipe. The experimental results of λ agree well with the theoretical result of (3.5) with a prefactor of 0.8 for all airflow conditions. Although δ is not directly resolved due to spatial-resolution limits of measurements, the consistency of the results with (3.5) demonstrates the validity of the theoretical expression for its velocity dependence. Similarly, the measured values of λ_p are consistent with the theoretical result with a prefactor of 4. This good agreement confirms that KH and RT instabilities form the three-dimensional ripple-wave structures

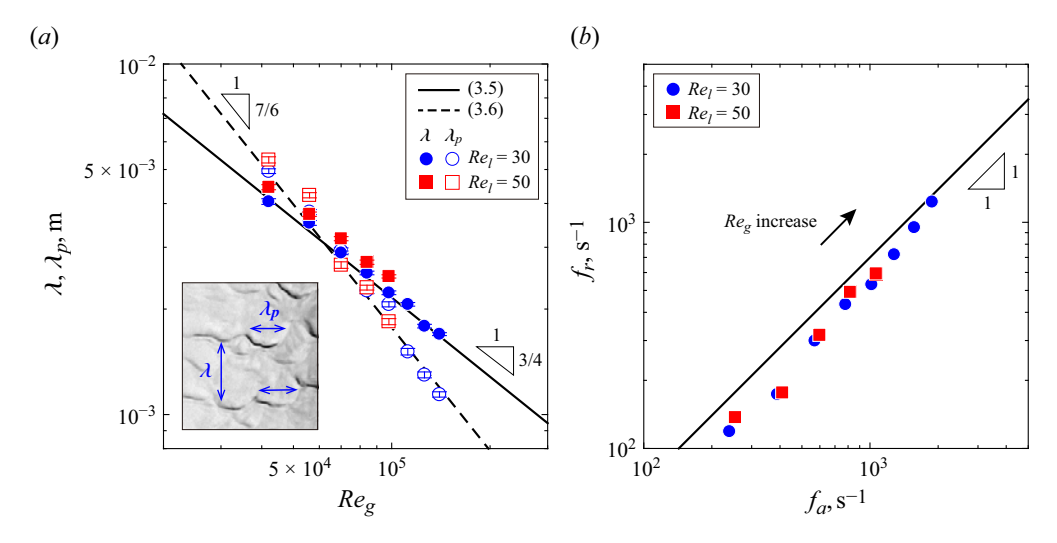


Figure 6. (a) Axial wavelength λ and circumferential wavelength λ_p of ripple waves as a function of Re_g . The solid lines and dashed lines present theoretical results given by (3.5) and (3.6), respectively. (b) Measured wave frequency f_r against theoretical value f_a of (3.8). The solid line depicts linear fit with a prefactor of 0.7.

on the liquid wall film, which demonstrates the complete analogy to a coaxial jet (Marmottant & Villermaux 2004). The effect of viscous damping is negligible under the present conditions of $Re_l > 10$ (Villermaux 1998).

The ripple wave propagates downstream with a phase velocity defined by Dimotakis (1986)

$$u_r = \frac{u_m \sqrt{\rho_l} + u_g \sqrt{\rho_g}}{\sqrt{\rho_l} + \sqrt{\rho_g}}.$$
(3.7)

Therefore, the wave frequency in the axial direction is

$$f_a = \frac{u_r}{\lambda}. (3.8)$$

Figure 6(b) shows the measured wave frequency f_r along with the theoretical value f_a . The experimental results are in good agreement with (3.8), thereby validating (3.7) as the phase velocity of ripple waves.

The wall film with ripple waves reaches the pipe end. As shown in figure 5(b), the liquid film temporarily stagnates on the trailing edge, from which cylindrical ligaments extend. In this situation, the stagnated liquid is accelerated into the lower-density gas phase by gas shear and gravity along the axial direction. This RT instability agitates the liquid mass in a unit circumferential wavelength of $m_t = 0.25\pi \rho_l h_t^2 \lambda_t$, and the surface area $0.5\pi h_t \lambda_t$ is subjected to the airflow. Using the acceleration a_t , the force balance per unit wavelength satisfies

$$m_t a_t \approx \frac{1}{2} \pi h_t \lambda_t \tau + m_t g. \tag{3.9}$$

For $\rho_l \gg \rho_g$, the most amplified RT instability wavelength is given by $\lambda_t \approx 2\pi \sqrt{3\sigma/(\rho_l a_t)}$ (Chandrasekhar 1961). We deduce the circumferential wavelength as follows:

$$\frac{\lambda_t}{h_t} \approx (f We_t + Bo_t)^{-0.5} \,. \tag{3.10}$$

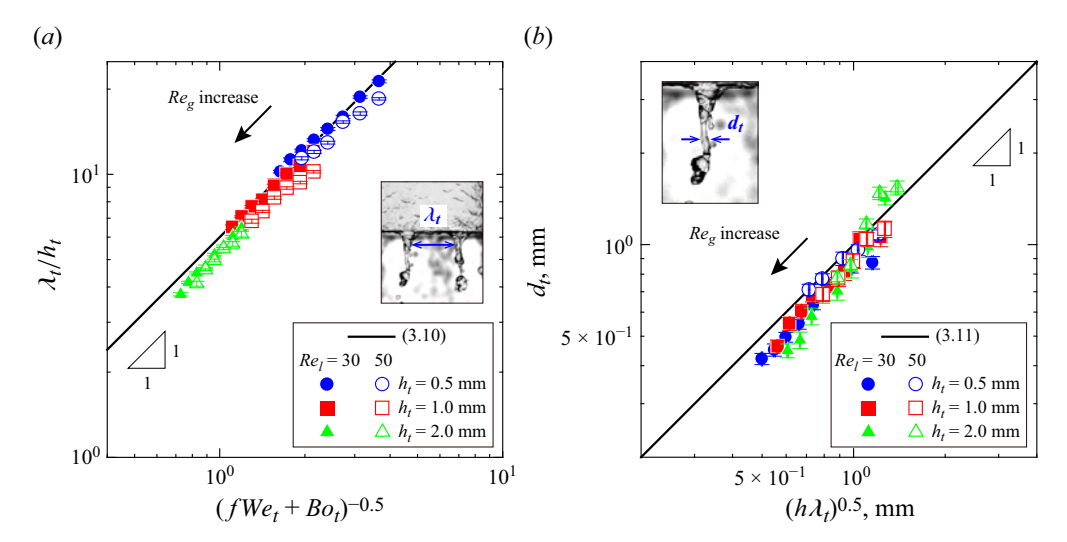


Figure 7. (a) Circumferential wavelength normalised by the trailing-edge thickness λ_t/h_t versus the nondimensional flow conditions at $h_t = 0.5$, 1.0 and 2.0 mm. The solid line shows (3.10) with a prefactor of 6. (b) Ligament diameter just before breakup d_t versus the square root of the liquid-film cross-sectional area. The solid line shows (3.11).

Here, we define the lip Weber number and the Bond number as $We_t = \rho_g u_g^2 h_t / \sigma$ and $Bo_t = \rho_l g h_t^2 / \sigma$, respectively. Figure 7(a) shows that (3.10) agrees well with the experimental results for all flow conditions and h_t , convincing that ligament elongation is stimulated by RT instability accelerated by gas shear and gravity. At high u_g , the gravitational term Bo_t becomes negligible, and ligament formation is driven solely by shear airflow.

In the ripple-wave regime, droplet entrainment from the film surface rarely occurs. As a result, the entire mass of the liquid film is drawn into the ligaments. Assuming that the elongation velocity of the ligament is equivalent to the film velocity, the film cross-sectional area per unit wavelength ($\sim h\lambda_t$) is equal to the ligament cross-sectional area ($\sim d_t^2$), leading to the ligament diameter of

$$d_t \approx \sqrt{h\lambda_t}. (3.11)$$

We measure the length l_t and projected area S of the ligaments just before breakup. Assuming a cylindrical shape, the average ligament diameter coincides with $d_t = S/l_t$. Figure 7(b) shows the experimental results for d_t against the cross-sectional film area per unit λ_t . Here, we theoretically calculate h using (3.2). For all h_t , we confirm the validity of (3.11). Moreover, (3.2) is also validated for estimating the mean thickness in the presence of ripple waves, as experimentally demonstrated by Kamada $et\ al.\ (2025c)$.

The positions of the ligaments remain almost stable throughout the breakup event. We measure the breakup period T as a time cycle for a droplet disintegration from a single ligament. The capillary time scale of the ligament is given by Chandrasekhar (1961)

$$\tau_{\sigma} \approx \sqrt{\frac{\rho_l d_t^3}{\sigma}}.$$
(3.12)

Figure 8(a) plots the measured breakup period T against τ_{σ} , calculated using experimental values of d_t . Breakup occurs more frequently as u_g increases and d_t decreases. We find a clear relationship $T \sim O(10^0)\tau_{\sigma}$, indicating that ligament breakup

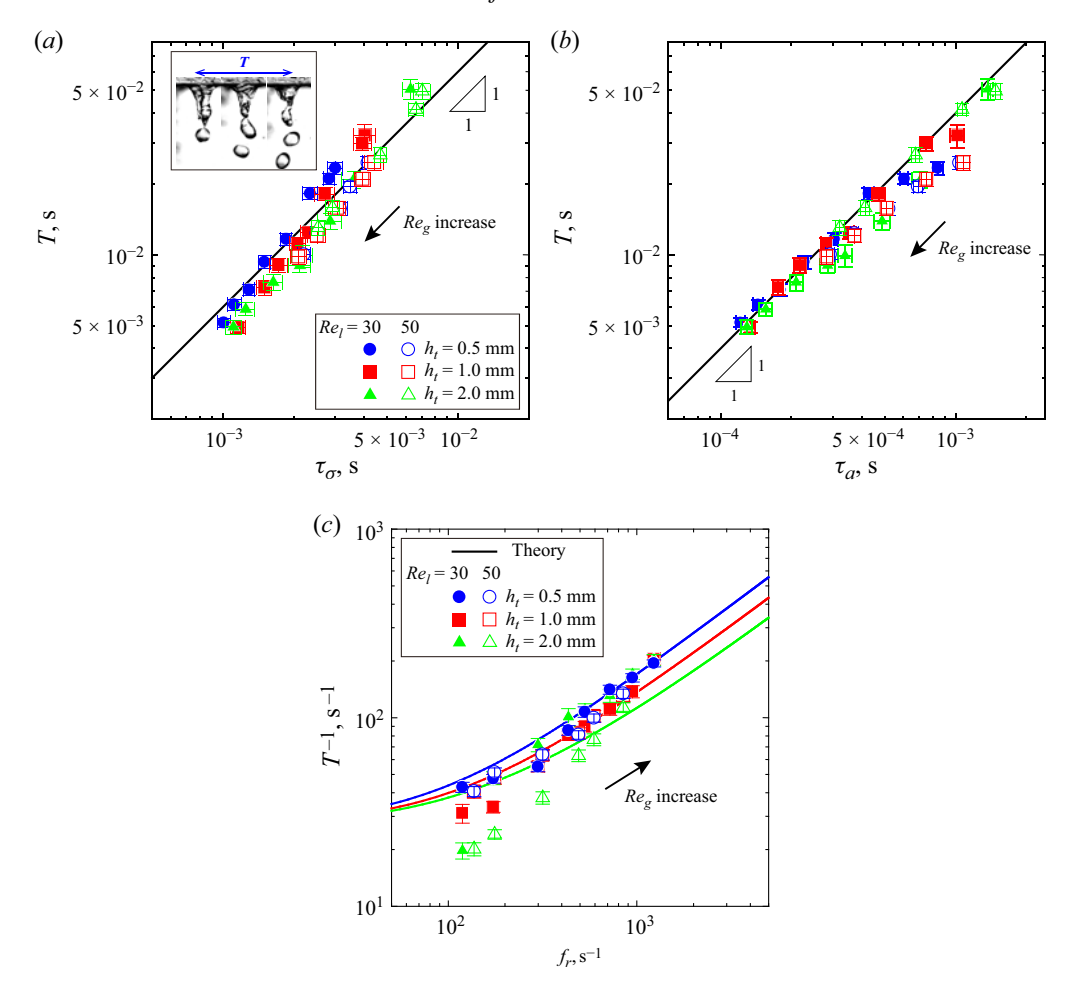


Figure 8. (a) Breakup period T versus capillary time τ_{σ} of ligament diameter d_t . The data collapse onto the line of $T \approx \tau_{\sigma}$ with a prefactor of 6. (b) Breakup period T versus aerodynamic shear time τ_a . The solid line shows linear fit with a prefactor of 40. (c) Frequency of ligament breakup T^{-1} versus ripple-wave frequency f_r . The solid line depicts the theoretical value of τ_{σ}^{-1} versus that of f_a for each h_t .

is a typical PR instability. We also compare the results with the time scale of aerodynamic shear $\tau_a = d_t/u_g\sqrt{\rho_l/\rho_g}$ in figure 8(b) (Nicholls & Ranger 1969), and find that $T \sim O(10^1)\tau_a$. This demonstrates that breakup proceeds at a much slower time scale of the aerodynamic shear, confirming the dominance of capillary effects, consistent with a previous study (Marmottant & Villermaux 2004).

Now, we connect the wall-film instability with the ligament breakup at the trailing edge. Figure 8(c) shows the experimental results for the ligament breakup frequency T^{-1} against the axial frequency of the ripple waves f_r . We find that the passing frequency of the ripple waves is approximately 10 times higher than the ligament breakup frequency, indicating that the influence of upstream liquid-film dynamics on the breakup event is relatively weak. Instead, the accumulation of liquid at the trailing edge plays a dominant role in the fragmentation of the liquid wall film accompanied by ripple waves. Consistently, h_t explicitly appears in the essential length scales of (3.10) and (3.11). We also confirm that the theoretical curve depicting τ_{σ}^{-1} in (3.12) against f_a in

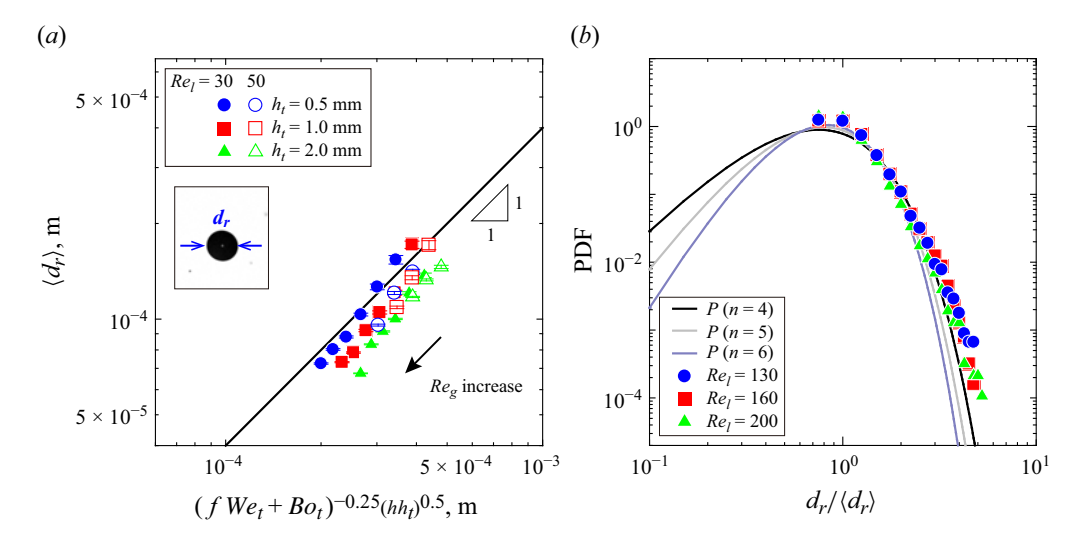


Figure 9. (a) Mean droplet diameter $\langle d_r \rangle$ against theoretical ligament diameter calculated by flow conditions. The solid line shows (3.13) with a prefactor of 0.4. (b) The PDF of droplet diameter normalised by the mean diameter at $u_g = 100 \text{ m s}^{-1}$ and $Re_l = 30$. The solid line shows the gamma distribution with $n = 4 \sim 6$.

(3.8) reproduces the experimental trend, well validating the aforementioned assumptions, including the interfacial friction factor on the ripple waves.

After fragmentation, subsequent secondary breakup rarely occurs, and a reasonable characteristic length scale for the arithmetic mean droplet diameter $\langle d_r \rangle$ is expected to be d_t as $\langle d_r \rangle \approx d_t$. By substituting (3.10) and (3.11), we deduce

$$\langle d_r \rangle \approx (f We_t + Bo_t)^{-0.25} (hh_t)^{0.5}.$$
 (3.13)

Figure 9(a) compares the experimental results for $\langle d_r \rangle$ with the theoretical ligament diameter. The good agreement validates (3.13), confirming that the mean diameter is predictable from the upstream flow conditions. Furthermore, the droplet-size distribution resulting from ligament breakup follows a gamma distribution with $n \gtrsim 4$ (Marmottant & Villermaux 2004; Villermaux 2007; Eggers & Villermaux 2008):

$$P(n, \xi = d_r/\langle d_r \rangle) = \frac{n^n}{\Gamma(n)} \xi^{n-1} e^{-n\xi}, \qquad (3.14)$$

where ξ is the droplet diameter normalized by $\langle d_r \rangle$, and $\Gamma(n)$ is the gamma function with factor n. Figure 9(b) shows a representative result at $Re_l = 30$ and $u_g = 100 \,\mathrm{m \, s^{-1}}$. The probability density function (PDF) of droplet diameters is plotted normalised by (3.13). For all trailing-edge thicknesses, the experimental PDFs are well represented by the gamma distribution with n = 4. We describe the complete sequences from the initiation of ripple waves to the final droplet formation.

As discussed earlier, the stagnation of liquid at the trailing edge is critical for the following steps. We then expect that the surface wettability on a thin trailing edge significantly changes the liquid accumulation on the trailing edge, as well as final droplet size (Kamada *et al.* 2025*b*), which is discussed in Appendix D.

3.3. Disturbance-wave regime

At We > 0.5, disturbance waves are superimposed on ripple waves on the liquid wall film. Figure 10(a) shows that a disturbance wave inside the pipe reaches the pipe end

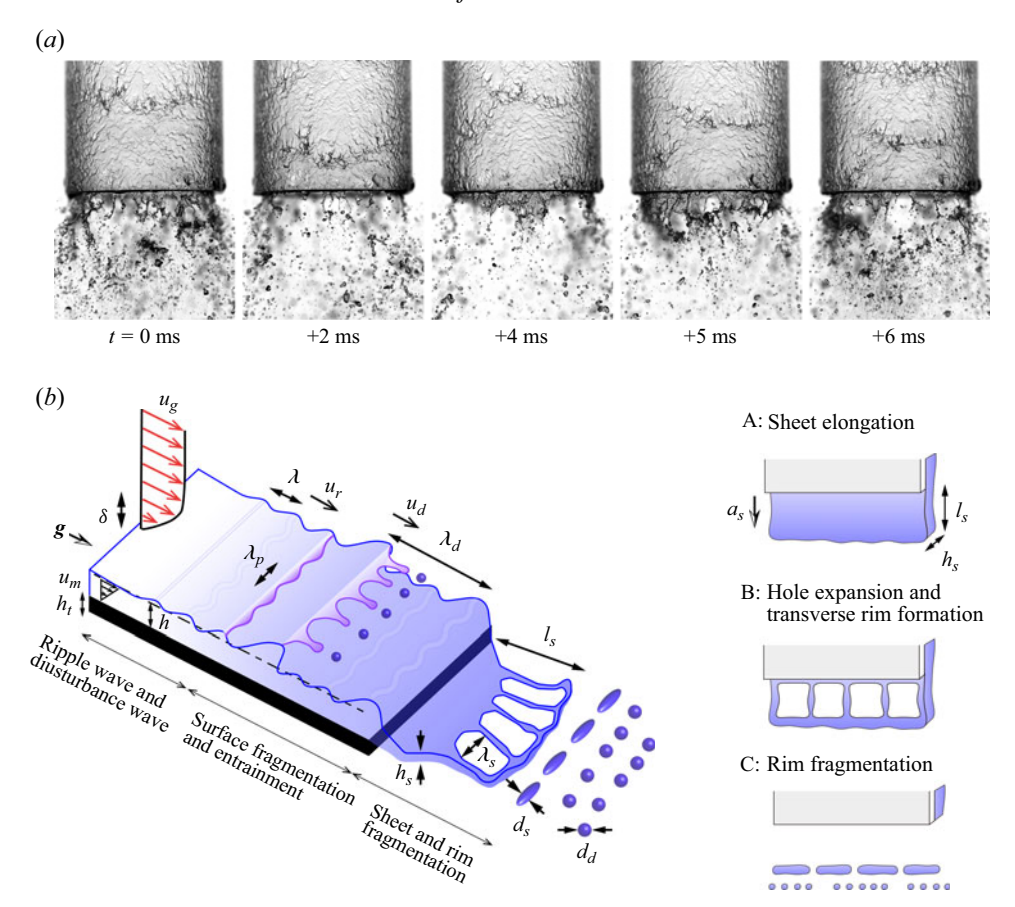


Figure 10. (a) Typical time series images of disturbance waves and sheet breakup at $Re_g = 1.3 \times 10^5$ and $Re_l = 130$. A disturbance wave observed on the wall surface at t = 0 ms deforms into a liquid sheet at t = 4 ms. At t = 5 ms, holes form on the sheet surface and rims at the tips, eventually collapsing into droplets. (b) Schematic diagram of film dynamics and fragmentation process in disturbance-wave regime.

and spontaneously emits in the form of a liquid sheet, undergoing hole formation, rim development at the sheet edges, and ultimately fragmentation into fine droplets. At t=+5 ms, the root of the ejected sheet connects to the wall film inside the pipe, not to the trailing edge. This observation is consistent with the previous study by Fukano (1988) that disturbance waves deliver liquid mass at a high velocity equivalent to the phase velocity. Figure 10(b) illustrates the sequence of these steps. The fully developed disturbance wave propagates downstream with an axial wavelength λ_d and phase velocity u_d . At the wave crest, the liquid film is stretched into a ligament, leading to droplet entrainment. As the disturbance wave reaches the trailing edge, it transforms into a free liquid sheet that elongates to a length l_s and thickness h_s . Subsequently, perforations form on the sheet surface and rapidly expand to a transverse length λ_s . The sheet then breaks into a rim with diameter d_s , which finally fragments into droplets with diameter d_d .

Figure 11(a) shows the experimental results for λ and λ_d at $Re_l = 130$, 160 and 200. We confirm that λ agrees well with the theoretical result of (3.5). The characteristics of ripple waves in the disturbance-wave regime are consistent with those in the ripple-wave regime. We find that λ_d is 10 times longer than λ , matching the wavelength of KH instability, which is independent of capillary effects. As discussed earlier, the onset

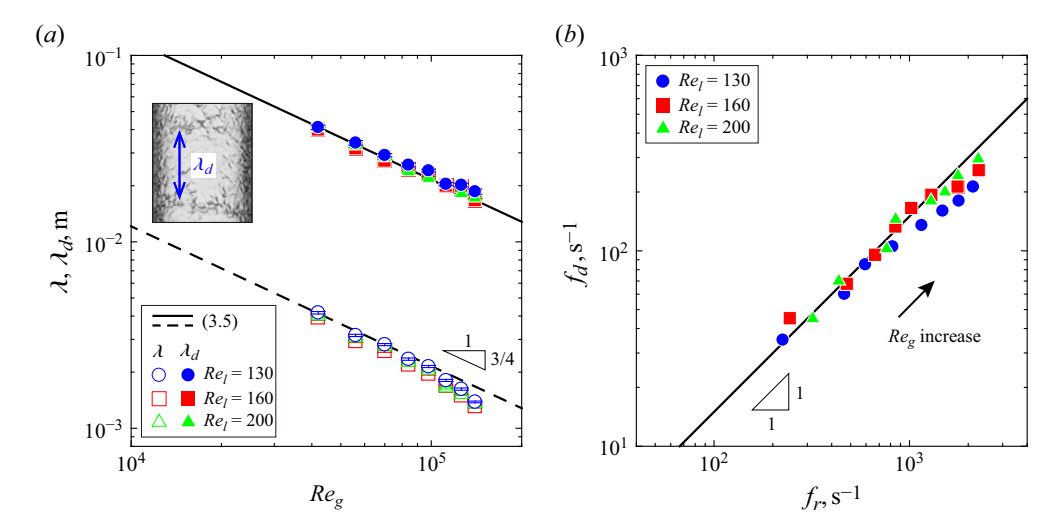


Figure 11. (a) Axial wavelength of ripple waves λ and of disturbance waves λ_d against Re_g . The solid and dashed lines show the theoretical results of (3.5) with prefactors of 8 and 0.8, respectively. (b) Frequency of disturbance waves f_d versus frequency of ripple waves f_r in the axial direction. The solid line depicts linear fit with a prefactor of 0.15.

of disturbance waves follows $We \approx 1$, where capillary effects are included. Perturbations amplify under the limited condition of We > 0.5, growing into long disturbance waves in approximately 10 ms due to KH instability. Figure 11(b) shows the experimental results for the disturbance-wave frequency f_d against the ripple wave frequency f_r . As disturbance waves appear less frequently, f_d is approximately 0.15 times f_r , while f_d also follows (3.8) as in the case of ripple waves. Hence, the phase velocity of disturbance waves also follows (3.7). These indicate that both ripple and disturbance waves are governed by the same mechanism, induced by KH instability. However, the underlying reason for the coexistence of the two successive instabilities has not yet been fully clarified. We assume that ripple waves modify the gas-side velocity boundary layer by introducing localised shear and vorticity variations, which may promote disturbance waves at a larger scale. Recent DNS reported that primary KH vortices can induce new thin shear layers, which subsequently become unstable and develop into secondary KH instabilities (Fritts et al. 2022).

At the pipe end, we measure the frequency of sheet breakup f_s . As shown in figure 12, f_s is nearly equivalent to f_d under all test conditions. This result suggests that disturbance waves transport liquid mass and periodically detach from the pipe end as liquid sheets. We clearly identify a direct connection between wall-film dynamics and downstream fragmentation in the disturbance-wave regime, which is distinct from the ripple-wave regime (see figure 8c). We also note that f_s can be directly calculated using (3.8).

As the liquid sheet stretches, holes appear in regions where the film is locally thin or impacted by scattered droplets (Villermaux 2020; Oshima & Sou 2024). These holes expand rapidly, forming rims along their edges. At low gas velocities in figure 13(a), the liquid sheet discharged from the pipe develops a bag structure at t = +6 ms. The thick transverse rim at the sheet edge (red arrow) produces large primary droplets, which subsequently undergo secondary atomization at t = +9.6 ms by aerodynamic forces, breaking up into finer droplets. At high gas velocities in figure 13(b), the transverse rim disintegrates earlier at t = +3 ms. In this case, the rim is sufficiently small that the resulting droplets disperse without further breakup.

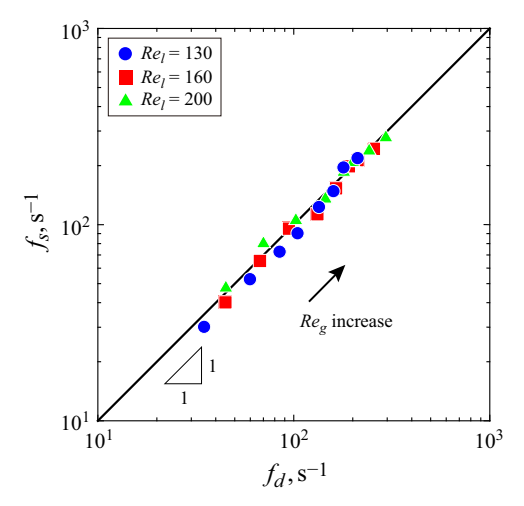


Figure 12. Sheet breakup frequency f_s versus disturbance wave frequency f_d . The solid line depicts $f_s = f_d$.

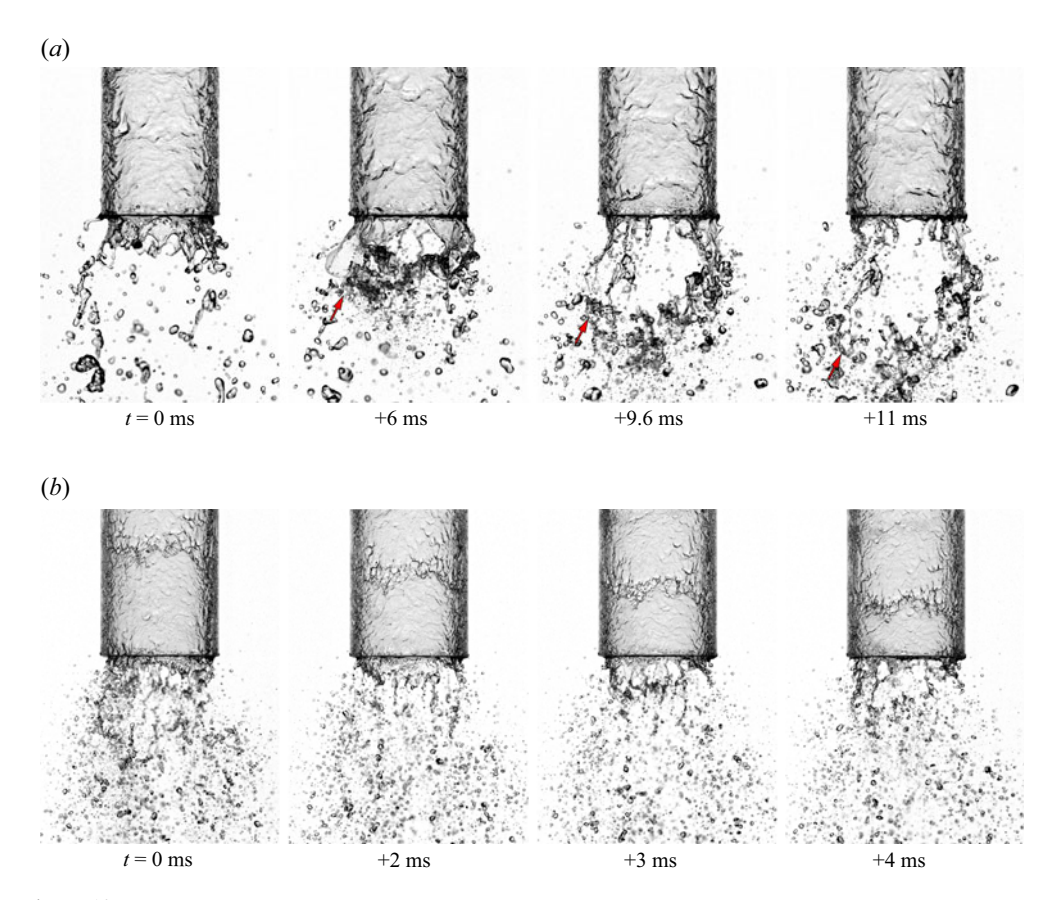


Figure 13. Time series images of fragmentation process in the disturbance-wave regime at $Re_l = 160$. (a) Here, $u_g = 30 \,\mathrm{m \, s^{-1}}$. The red arrows indicate rim breakup events accompanied by bag formation, which subsequently undergo secondary atomization. (b) Here, $u_g = 60 \,\mathrm{m \, s^{-1}}$ without secondary breakup.

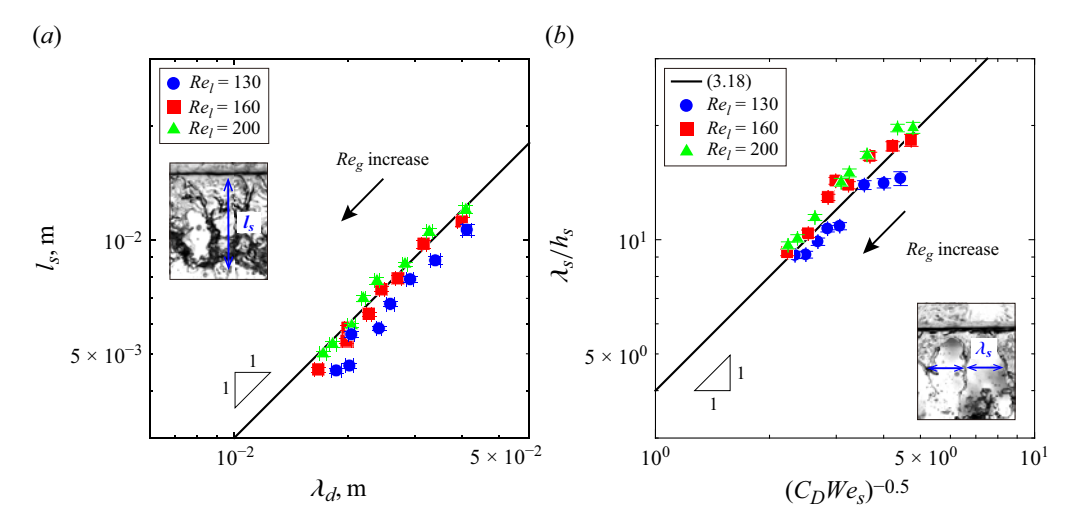


Figure 14. (a) Maximum sheet length l_s against wavelength of disturbance wave λ_d . The solid line depicts $l_s \approx \lambda_d$ with a prefactor of 0.3. (b) Circumferential wavelength normalised by sheet thickness λ_s/h_s versus dimensionless flow conditions. The solid line shows (3.18) with a prefactor of 4.

Figure 14(a) compares the maximum l_s just before breakup with λ_d . Since l_s is approximately equivalent to λ_d , the liquid mass transported by a single disturbance wavelength is directly ejected as a liquid sheet containing the same amount of mass. We observe droplet entrainment from the crests of disturbance waves, whereas sheet breakup at the trailing edge is the primary mechanism of droplet dispersion. For simplicity, we assume that the ejected liquid sheet has a uniform thickness h_s at its maximum length, as shown in figure 10(b). By applying the conservation of flow rate between the liquid film entering the pipe and the liquid sheet discharged from the pipe end, we obtain the following equation:

$$Q_l = \pi D_l l_s h_s f_s. \tag{3.15}$$

Thus, h_s is given by a function of Re_l as

$$h_s = \frac{Re_l \ v_l}{l_s \ f_s}.\tag{3.16}$$

The liquid sheet oscillates perpendicular to the airflow in the radial direction and accelerates by aerodynamic forces, leading to RT instability. Introducing the drag coefficient C_D , the acceleration of the ejected sheet a_s is given by

$$a_s = \frac{\frac{1}{2}C_D \rho_g u_g^2}{\rho_l h_s}. (3.17)$$

Following the previous study by Varga *et al.* (2003), we employ $C_D = 2$. By substituting into the most unstable wavelength of RT instability, the circumferential wavelength λ_s is derived as

$$\frac{\lambda_s}{h_s} \approx 2\pi \sqrt{6} (C_D We_s)^{-0.5}. \tag{3.18}$$

Here, the sheet Weber number is defined as $We_s = \rho_g u_g^2 h_s / \sigma$. Figure 14(b) shows the experimental results of the normalised wavelength against the dimensionless flow

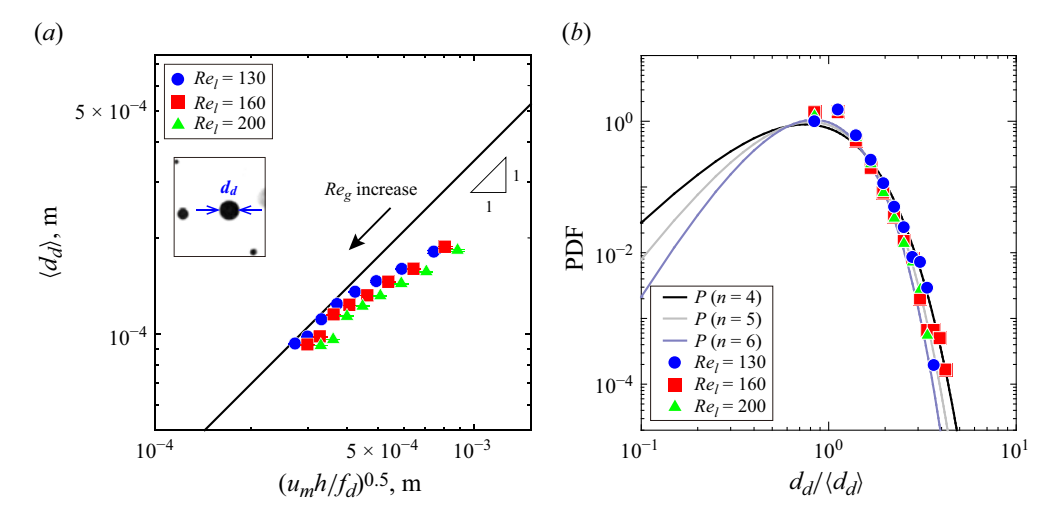


Figure 15. (a) Mean droplet diameter $\langle d_d \rangle$ against theoretical rim diameter. The solid line shows (3.20) with a prefactor of 0.35. (b) The PDF of droplet diameter normalised by the mean diameter at $u_g = 100 \text{ m s}^{-1}$. The solid line presents the gamma distribution with $n = 4 \sim 6$.

conditions. We estimate the sheet thickness h_s using (3.16) combined with the measured l_s and f_s . The experimental results follow the theoretical result, thus validating the proposed model. Therefore, the circumferential waves observed on the elongating liquid sheet are attributed to RT instability, consistent with previous studies (Chaussonnet *et al.* 2016; Choi *et al.* 2022). We also observe that the trailing-edge thickness h_t does not appear, indicating that the wall film does not accumulate on the pipe end in this disturbance-wave regime, consistent with the visualisation results in figure 10(a). The effect of trailing-edge configuration becomes less important than in the ripple-wave regime.

Based on the rim formation process, volume conservation between the liquid sheet and the rim per unit circumferential wavelength yields the rim diameter d_s as

$$d_s \approx \sqrt{\frac{Re_l \, \nu_l}{f_s}}.\tag{3.19}$$

Reasonably assuming that the final droplet diameter is proportional to d_s , we finally obtain the mean droplet diameter $\langle d_d \rangle$.

$$\langle d_d \rangle \approx \sqrt{\frac{u_m h}{f_d}}$$
 (3.20)

Figure 15(a) compares the experimental results of $\langle d_d \rangle$ with the theoretical result. When the airflow is high at $u_g \geq 50 \,\mathrm{m\,s^{-1}}$, (3.20) is valid for all Re_l conditions with a prefactor of 0.35 and provides the mean diameter based on the upstream flow conditions. The liquid topology changes such that the liquid wall film inside the pipe with a cross-sectional area along the axial direction of $u_m h/f_d$ changes into a transverse ligament with an equivalent cross-section of d_s^2 , which subsequently breaks up into droplets. In this disturbance-wave regime, the transverse ligament aligned perpendicular to the flow direction provides the characteristic length scale for the droplets (Dombrowski & Johns 1963; Kooij *et al.* 2018), in contrast to the ripple-wave regime, where the axial ligaments elongated along the streamwise direction are critical for droplet formation. At $u_g < 50 \,\mathrm{m\,s^{-1}}$, however, the

theoretical result overestimates the measured droplet size. This discrepancy is attributed to the formation of a thick rim, which is subjected to secondary atomization downstream (see figure 13a). From (3.19), the rim diameter is estimated as $d_s \approx O(10^{-3})$ m, resulting in a Weber number of $\rho_g u_g^2 d_s / \sigma \approx O(10^1)$. Consequently, the droplet size after secondary breakup becomes smaller than the original rim diameter. Figure 15(b) shows the PDF of the droplet size normalised by (3.20) at $u_g = 100 \text{ m s}^{-1}$. For all Re_l , the PDF consistently represents a gamma distribution with n = 4, thereby completing the scenario for the disturbance-wave regime.

4. Conclusion

We experimentally and theoretically examined a series of phenomena, from annular wall-film dynamics to fragmentation, under well-controlled boundary conditions involving a uniform liquid film subjected to a fully developed turbulent airflow. Through comprehensive experiments, we identified two distinct flow regimes of film flow as the ripple-wave regime and disturbance-wave regime, by defining a new criterion as the liquid-film Weber number of unity. For each regime, we successfully developed distinct theoretical models that quantitatively link wall-film instabilities to droplet statistics, which were well validated by the experimental results. We demonstrated the mathematically consistent analogy between the axial jet instabilities and those of the wall film.

In the ripple-wave regime of We < 0.5, three-dimensional ripple waves form by the superposition of KH instability in the axial direction and RT instability in the transverse direction. When the liquid wall film reaches the nozzle exit, it accumulates on the trailing edge, from which isolated ligaments extend periodically arranged along the circumferential direction due to RT instability. Diameter of the axial ligament is directly proportional to the size of resulting droplets, preserving information about the trailing-edge thickness. The breakup frequency of the ligaments is one-tenth that of the ripple waves, representing a weak coupling between liquid-film instability and the subsequent fragmentation process. In the disturbance-wave regime of We > 0.5, long and fast disturbance waves emerge, following the same KH instability mechanism as short and slow ripple waves. When the disturbance waves reach the trailing edge, a liquid sheet is spontaneously ejected. At the sheet edges, transverse rims form via RT instability and subsequently fragment into fine droplets. Equivalence of the frequencies between the disturbance waves and the sheet breakup provides clear evidence that upstream wall-film instabilities directly influence the fragmentation process.

While the present study discusses the annular flow dynamics, the underlying mechanisms are likely applicable to wall films on flat plates, wings and in nozzle flows. Incorporating wall-film dynamics typically in the disturbance-wave regime into numerical and theoretical models can improve the prediction accuracy of discharged droplet size. This is beneficial in cases involving droplet erosion issues caused by coarse droplets, such as in steam turbines.

Supplementary movie. Supplementary movie is available at https://doi.org/10.1017/jfm.2025.10869.

Acknowledgements. We thank Dr S. Senoo (Mitsubishi Heavy Industries, Ltd) for his valuable comments on the droplet erosion issue.

Funding. This work was supported by JST SPRING (Grant Number JPMJSP2136) and by JSPS KAKENHI (Grant Number JP24K00806).

Declaration of interests. The authors report no conflict of interest.

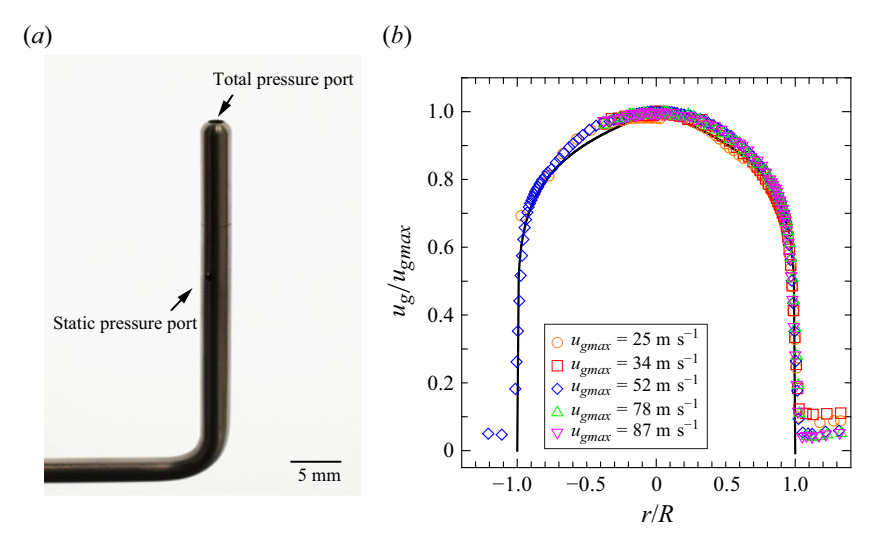


Figure 16. (a) Pitot tube with a total pressure port located at the top, and three static pressure ports on the side. (b) Velocity profile of airflow at the outlet of the stainless steel pipe along the radial direction at 25 m s⁻¹ $\leq u_{gmax} \leq 87$ m s⁻¹.

Appendix A. Velocity profile of gas jet

The airflow enters the test section through the stainless steel pipe to become fully developed. To confirm the velocity profile of the airflow inside the acrylic pipe, we measure the distribution of total pressure using a Pitot tube (figure 16a) along the radial direction at 1 mm away from the pipe exit. The probe of 3 mm in diameter has a total pressure port at the top and three static pressure ports on the side, mounted on a traversing device to move horizontally at every 0.1 mm. The pressure is measured by a pressure sensor (DP15, Validyne) with a relative measurement error of 0.5 %.

Figure 16(b) shows the experimental results as well as the theoretical curve of the power law following

$$\frac{u_g}{u_{gmax}} = \left[1 - \left(\frac{r}{R}\right)\right]^{\frac{1}{n}},\tag{A1}$$

where u_{gmax} is the central gas velocity, r is the radial distance, and $R = 0.5D_g$ is the pipe radius. The measured velocity profile shows good agreement with the theoretical profile for n = 7, confirming that the airflow becomes a fully developed turbulent flow at all mean velocities.

Appendix B. Droplet-size analysis

We conduct image analysis using the open-source software ImageJ. Based on the image processing technique illustrated in figure 17(a), we selectively identify in-focus droplets. The procedure consists of the following steps. (i) A background image is subtracted from an image capturing droplets to eliminate background noise. (ii) We apply a Gaussian filter with a standard deviation of $\sigma_G = 1$ pixel. The edges of out-of-focus droplets are less affected by this filtering process. (iii) By subtracting the Gaussian-filtered image from the image in step (i), the outlines of in-focus droplets remain, while out-of-focus droplets diminish. The resulting image is then binarised using an appropriate threshold.

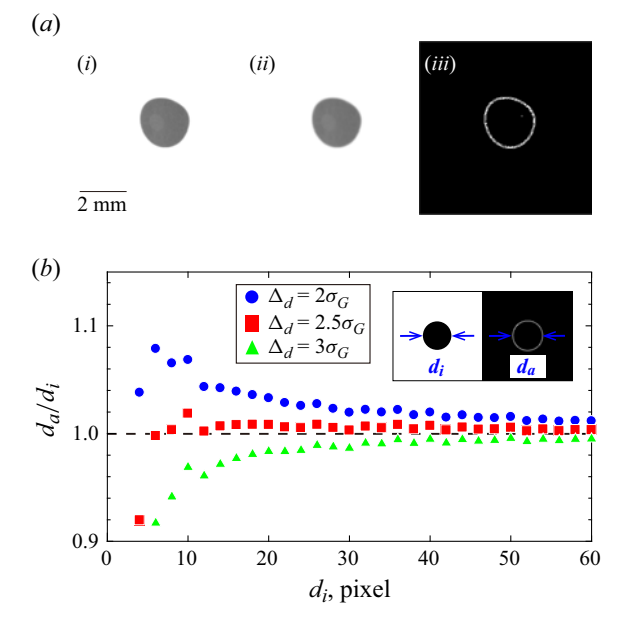


Figure 17. (a) Image processing steps for identifying in-focus droplets: (i) background-subtracted image; (ii) result of applying a Gaussian filter to (i); (iii) difference image by subtracting (ii) from (i). (b) Ratio of measured diameters d_a to true diameters d_i at three subtraction lengths of Δ_d .

The projected area S of each droplet is measured to calculate the area-equivalent diameter as $\sqrt{4S/\pi}$.

To correct the bias due to the Gaussian filter, we subtract a fixed number of pixels Δ_d from the area-equivalent diameter. To evaluate the effect of filtering and determine an appropriate correction, we measure the circle diameters as $d_a = \sqrt{4S/\pi} - \Delta_d$ for known diameters d_i ranging from 4 to 60 pixels. As shown in figure 17(b), the case of $\Delta_d = 2.5\sigma_G$ pixels yields the highest accuracy, with a mean error of 0.4% and a maximum overestimation of 1.9% for circles larger than 6 pixels. We consistently employ a Gaussian filter width of $\sigma_G = 1$ pixel and a post-subtraction length of $\Delta_d = 2.5$ pixels. For threshold values, we set the minimum circularity at 0.8 and the minimum droplet diameter at 6 pixels.

Appendix C. Film thickness

We measure the liquid-film thickness sheared by the airflow using brightness-based laser induced fluorescence (BBLIF) by dissolving rhodamine B dye in the working liquid of water. As shown in figure 18(a), a laser light source (wavelength $\lambda_L = 532$ nm) is directed onto the test section to induce fluorescence from the same direction as the camera. A long-pass filter that transmits wavelengths above 550 nm is attached to the lens to selectively record the fluorescence emission at approximately 570 nm.

The film thickness is calculated from the fluorescence intensity based on the Beer–Lambert law. When the film is sufficiently thin to avoid significant attenuation, the instantaneous thickness is proportional to the local pixel brightness I(x, y, t) (Cherdantsev *et al.* 2023):

$$h(x, y, t) = a(x, y)I(x, y, t).$$
 (C1)

Here, a(x, y) is the regression coefficient. We perform calibration to determine a(x, y) at a gravity-driven vertical falling film flow without the airflow (see figure 1b) for

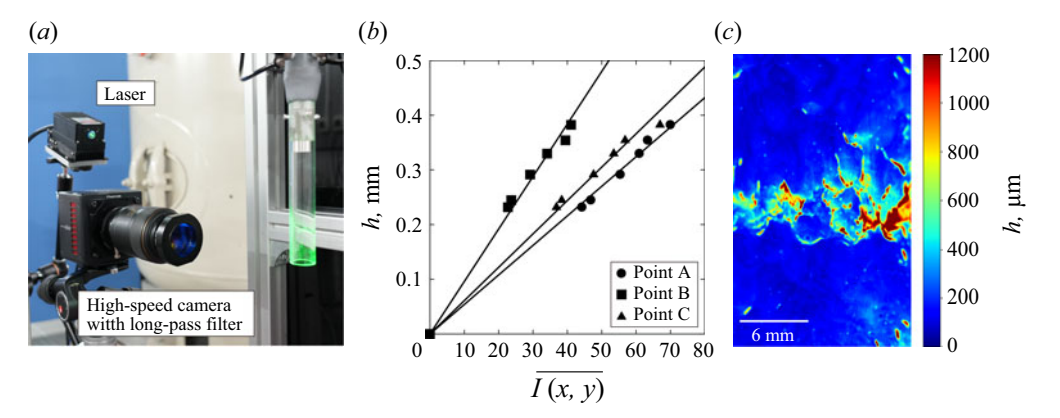


Figure 18. (a) Experimental set-up of the imaging system for BBLIF. (b) Theoretical film thickness h in (C2) against $\overline{I(x, y)}$ at three different points. The gradient of each line represents the prefactor of a(x, y). (c) BBLIF result showing disturbance waves at $Re_l = 160$ and $u_g = 70$ m s⁻¹. Flow direction is downward.

 $Re_l = 20-200$. At a steady state, the film thickness follows the theoretical solution:

$$h = \left(\frac{3Re_l v_l^2}{g}\right)^{1/3}.$$
 (C2)

As shown in figure 18(b), h exhibits a linear correlation with the time-averaged brightness $\overline{I(x, y)}$, providing $a(x, y) = h/\overline{I(x, y)}$ at every pixel. The linearity validates the calibrated a(x, y) for film thickness of thinner than 0.4 mm, which satisfies the present experiment.

Figure 18(c) shows a representative result of instantaneous thickness distribution in the disturbance-wave regime. Red area corresponds to the crests of disturbance waves with large amplitudes, while blue area shows the thin film. This demonstrates that the BBLIF method can effectively reconstruct the three-dimensional wave structure.

Under the conditions with the central airflow, we record the fluorescence from liquid film at 1000 f.p.s. for 2 s to measure the mean film thickness $h_{Exp.}$, defined as the time-averaged thickness over the region of interest, i.e.

$$h_{Exp.} = \frac{\sum \overline{h(x, y)}}{N_{xy}},\tag{C3}$$

where N_{xy} is the number of pixels. As shown in figure 19(a), $h_{Exp.}$ agrees well with the theoretical value calculated by (3.2) in both regimes of ripple wave and disturbance wave. Based on (3.1) and (3.2), we deduce the interfacial friction factor $f_{Exp.}$ as

$$f_{Exp.} = 4 \frac{\rho_g}{\rho_l} \left(\frac{\mu_l}{\mu_g}\right)^2 Re_{gf}^{-2} Re_l - \frac{4}{3} \frac{\rho_l}{\rho_g} Fr^{-2}.$$
 (C4)

Here, the film Reynolds number and Froude number are defined as $Re_{gf} = \rho_g u_g h/\mu_g$ and $Fr = u_g/\sqrt{gh}$. The measured film thickness is substituted into (C4) to calculate $f_{Exp.}$. Figure 19(b) depicts that $f_{Exp.}$ coincides with the Blasius correlation within $\pm 20 \%$ deviation. Therefore, we can reasonably employ the Blasius correlation for the analysis of ripple and disturbance waves. At higher Re_g conditions, however, $f_{Exp.}$ decreases sharply. This trend arises because intense surface deformation enhances interfacial reflections of fluorescence, leading to a local overestimation of the film thickness (see the wave crest

Y. Kamada, Z. Wang and C. Inoue

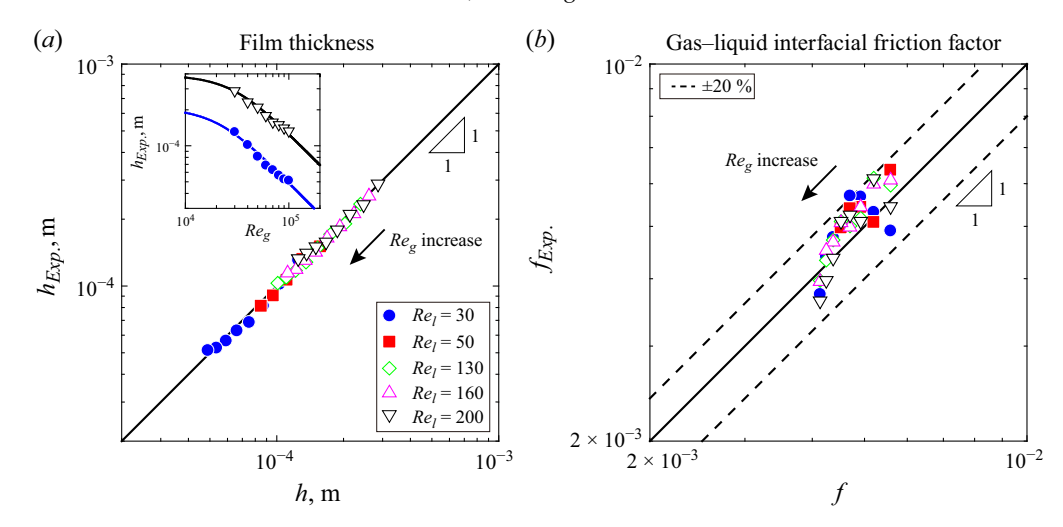


Figure 19. (a) Experimental film thickness $h_{Exp.}$ versus the theoretical results of (3.2). Filled symbols correspond to the ripple-wave regime, while open symbols represent the disturbance-wave regime. The inset shows film thickness as a function of Re_8 . (b) Experimental interfacial friction factor $f_{Exp.}$ versus the Blasius correlation f. The dashed lines indicate a deviation of $\pm 20\%$ from the relation of $f_{Exp.} = f$.

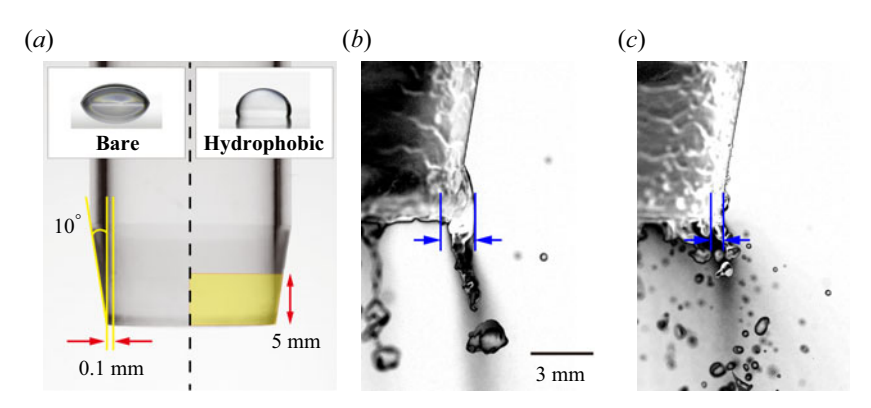


Figure 20. (a) Sharp-cut trailing edge with tip thickness $h_t = 0.1$ mm for two types of outer surface: bare and hydrophobic. The yellow-shaded area indicates the hydrophobic area, coated circumferential for 5 mm from the bottom edge. Instantaneous snapshots superimposed on time-averaged images at $Re_l = 30$ and $Re_g = 8.4 \times 10^4$ for (b) bare surface and for (c) hydrophobic surface. The blue arrows depict the liquid thickness adhering on the pipe outside.

in figure 18c), as reported previously (Alekseenko et al. 2014). When Fr is negligible in (C4), we deduce $f_{Exp.} \propto h^{-2}$. Even slight overestimation of h directly reduces $f_{Exp.}$.

Appendix D. Effect of surface wettability

In the ripple-wave regime, we conduct experiments by varying the surface wettability on the sharp-cut pipe end (for detail see Kamada *et al.* 2025*b*). As illustrated in figure 20(*a*), the trailing edge has an inclined angle of 10° and an edge thickness of $h_t = 0.1$ mm. In the hydrophobic case, a coating of FS-1610 is applied to the outer wall over a 5 mm region from the bottom end of the pipe. The static contact angle is 60° on the bare surface, whereas the contact angle increases to 120° on the hydrophobic surface.

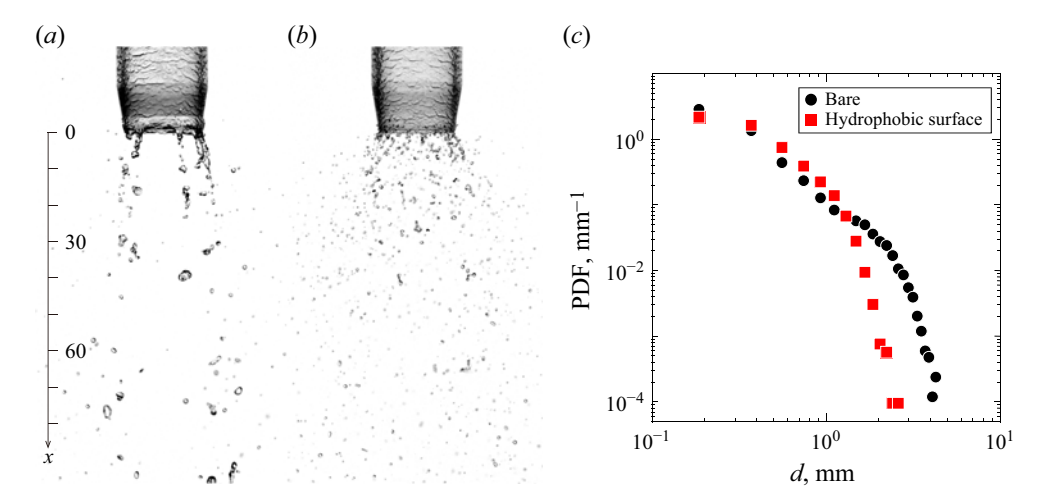


Figure 21. Overall visualisation results at $Re_l = 30$ and $Re_g = 8.4 \times 10^4$ for (a) bare case and for (b) hydrophobic case. (c) Dimensional droplet size distribution measured at x = 200 mm.

Figure 20(b,c) shows instantaneous snapshots close to the trailing edge superimposed on time-averaged images in 2 s. For the bare surface shown in figure 20(b), the thick film covers the outer wall, from which the ligament extends with a diameter larger than h_t . The dark streaks in the background represent droplet trajectories. These trajectories appear periodically along the circumferential direction, stimulated by the RT instability as visible in figure 5(a). In contrast, for the hydrophobic surface, the adhesion on the outer wall is clearly suppressed, resulting in the short ligaments with dense distribution attached to the thin bottom edge.

Figure 21(a,b) represents the overall visualisation of droplet dispersion downstream up to x < 100 mm at $Re_l = 30$ and $Re_g = 8.4 \times 10^4$ ($u_g = 60 \text{ m s}^{-1}$). For the bare surface in figure 21(a), some drops remain the original size split from the thick ligaments on the trailing edge, while partial drops break up downstream by being exposed to the central jet. Contrary, the hydrophobic pipe clearly produces a large number of fine droplets spreading widely in the radial direction in figure 21(b). We show in figure 21(c) the droplet size distribution at x = 200 mm measured by a spatial resolution of $30 \,\mu\text{m}$ pixel⁻¹. Coarse drops up to d = 4 mm in diameter exist for the bare case, while the maximum size decreases to $d \approx 2$ mm for the hydrophobic case with narrower distribution attributed to the initially thin ligaments on the edge. We demonstrate that the hydrophobic coating at the trailing edge effectively reduces the film adhesion, leading to the finer droplet size.

REFERENCES

ALEKSEENKO, S.V., CHERDANTSEV, A.V., HEINZ, O.M., KHARLAMOV, S.M. & MARKOVICH, D.M. 2014 Analysis of spatial and temporal evolution of disturbance waves and ripples in annular gas—liquid flow. *Intl J. Multiphase Flow* 67, 122–134.

ALEKSEENKO, S.V. & NAKORYAKOV, V.E. 1995 Instability of a liquid film moving under the effect of gravity and gas flow. *Intl J. Heat Mass Transfer* 38 (11), 2127–2134.

ANDREUSSI, P., ASALI, J.C. & HANRATTY, T.J. 1985 Initiation of roll waves in gas-liquid flows. *AIChE J.* **31** (1), 119–126.

AZZOPARDI, B.J. 1997 Drops in annular two-phase flow. Intl J. Multiphase Flow 23 (7), 1-53.

BERNA, C., ESCRIVÁ, A., MUÑOZ-COBO, J.L. & HERRANZ, L.E. 2014 Review of droplet entrainment in annular flow: interfacial waves and onset of entrainment. *Prog. Nucl. Energy* 74, 14–43.

BOZONNET, C., MATAS, J.P., BALARAC, G. & DESJARDINS, O. 2022 Stability of an air—water mixing layer: focus on the confinement effect. *J. Fluid Mech.* 933, A14.

Y. Kamada, Z. Wang and C. Inoue

- CHANDRASEKHAR, S. 1961 Hydrodynamic and Hydromagnetic Stability. Courier Corporation.
- CHAUSSONNET, G., VERMOREL, O., RIBER, E. & CUENOT, B. 2016 A new phenomenological model to predict drop size distribution in Large-Eddy Simulations of airblast atomizers. *Intl J. Multiphase Flow* **80**, 29–42.
- CHERDANTSEV, A.V. 2023 Three-dimensional evolution and interaction of disturbance waves on a gassheared liquid film on a horizontal plane near the transition region. *Intl J. Multiphase Flow* **164**, 104468
- CHERDANTSEV, A., BOBYLEV, A., GUZANOV, V., KVON, A. & KHARLAMOV, S. 2023 Measuring liquid film thickness based on the brightness level of the fluorescence: methodical overview. *Intl J. Multiphase Flow* 168, 104570.
- CHERDANTSEV, A., ISAENKOV, S. & MARKOVICH, D. 2025 Transition to entrainment in downward annular gas—liquid flow: study through flow control. *Intl J. Multiphase Flow* **184**, 105109.
- CHOI, D., BYUN, J. & PARK, H. 2022 Analysis of liquid column atomization by annular dual-nozzle gas jet flow. J. Fluid Mech. 943, A25.
- CROWE, C.T. 2005 Multiphase Flow Handbook. CRC press.
- DIMOTAKIS, P.E. 1986 Two-dimensional shear-layer entrainment. AIAA J. 24 (11), 1791–1796.
- DOMBROWSKI, N. & FRASER, R.P. 1954 A photographic investigation into the disintegration of liquid sheets. *Phil. Trans. R. Soc. Lond. A* **247** (924), 101–130.
- DOMBROWSKI, N. & JOHNS, W.R. 1963 The aerodynamic instability and disintegration of viscous liquid sheets. *Chem. Engng Sci.* **18** (3), 203–214.
- EGGERS, J. & VILLERMAUX, E. 2008 Physics of liquid jets. Rep. Prog. Phys. 71 (3), 036601.
- EPSTEIN, M. 1990 Theory of scrubbing of a volatile fission product vapor-containing gas jet in a water pool. In ANS sixth proceedings of the nuclear thermal hydraulics, American Nuclear Society.
- FRITTS, DAVID C., WANG, L., LUND, T.S. & THORPE, S.A. 2022 Multi-scale dynamics of Kelvin-Helmholtz instabilities. Part 1. Secondary instabilities and the dynamics of tubes and knots. *J. Fluid Mech.* **941**, A30.
- FUKANO, T. 1988 Mechanism of the disturbance wave generation in a vertical up-and down-ward gas—liquid two-phase annular flow. In *Transient Phenomena in Multiphase Flow*, pp. 435–452.
- GUILDENBECHER, D.R., LÓPEZ-RIVERA, C. & SOJKA, P.E. 2009 Secondary atomization. *Exp. Fluids* 46 (3), 371–402.
- HEWITT, G.F. & ROBERTS, D.N. 1969 Studies of two-phase flow patterns by simultaneous x-ray and flast photography. *Tech. Rep.*. Atomic Energy Research Establishment, Harwell, England (United Kingdom).
- HUTCHINSON, P. & WHALLEY, P.B. 1973 A possible characterization of entrainment in annular flow. Chem. Engng Sci. 28, 974–975.
- INAMURA, T., KATAGATA, N., NISHIKAWA, H., OKABE, T. & FUMOTO, K. 2019 Effects of prefilmer edge thickness on spray characteristics in prefilming airblast atomization. *Intl J. Multiphase Flow* 121, 103117.
- INOUE, C. & MAEDA, I. 2021 On the droplet entrainment from gas-sheared liquid film. *Phys. Fluids* 33 (1), 011705.
- INOUE, T., INOUE, C., FUJII, G. & DAIMON, Y. 2022 Evaporation of three-dimensional wavy liquid film entrained by turbulent gas flow. *AIAA J.* **60** (6), 3805–3812.
- ISAENKOV, S.V., CHERDANTSEV, A.V., VOZHAKOV, I.S., CHERDANTSEV, M.V., ARKHIPOV, D.G. & MARKOVICH, D.M. 2019 Study of primary instability of thick liquid films under strong gas shear. *Intl J. Multiphase Flow* 111, 62–81.
- ISHII, M. & GROLMES, M.A. 1975 Inception criteria for droplet entrainment in two-phase concurrent film flow. AIChE J. 21 (2), 308–318.
- ISHII, M. & HIBIKI, T. 2010 Thermo-Fluid Dynamics of Two-Phase Flow. Springer Science & Business Media.
- JACKIW, I.M. & ASHGRIZ, N. 2022 Prediction of the droplet size distribution in aerodynamic droplet breakup. J. Fluid Mech. 940, A17.
- JACKIW, I.M. & ASHGRIZ, N. 2023 Aerodynamic droplet atomization model (ADAM). J. Fluid Mech. 958, A2.
- JIANG, D. & LING, Y. 2021 Impact of inlet gas turbulence on the formation, development and breakup of interfacial waves in a two-phase mixing layer. J. Fluid Mech. 921, A15.
- KAMADA, Y., MURAKAMI, K., WANG, Z., INOUE, C. & SENOO, S. 2025a Relationship between wavy liquid film dynamics and droplet formation from trailing edge. J. Engng Gas Turbines Power 147 (3), 031014.
- KAMADA, Y., MURAKAMI, K., WANG, Z., INOUE, C. & SENOO, S. 2025b Suppression of coarse droplet formation from gas-sheared liquid sheets by controllingthe trailing edge shape and wettability. *J. Engng Gas Turbines Power* 148 (2), 031006.
- KAMADA, Y., WANG, Z., INOUE, C. & SENOO, S. 2025c Time-variant planar laser-induced fluorescence for thickness measurement of wavy liquid films: a calibration-free and threshold-free method. Exp. Fluids 66 (3), 58.

- KOOIJ, S., SIJS, R., DENN, M.M., VILLERMAUX, E. & BONN, D. 2018 What determines the drop size in sprays? *Phys. Rev. X* 8 (3), 031019.
- KULKARNI, V., SHIRDADE, N., RODRIGUES, N., RADHAKRISHNA, V. & SOJKA, P.E. 2023 On interdependence of instabilities and average drop sizes in bag breakup. *Appl. Phys. Lett.* **123** (2), 024101.
- LE CORRE, J.M. 2022 Phenomenological model of disturbance waves in annular two-phase flow. *Intl J. Multiphase Flow* **151**, 104057.
- LHUISSIER, H. & VILLERMAUX, E. 2013 'Effervescent' atomization in two dimensions. J. Fluid Mech. 714, 361–392.
- MARMOTTANT, P. & VILLERMAUX, E. 2004 On spray formation. J. Fluid Mech. 498, 73-111.
- MATAS, J.P., DELON, A. & CARTELLIER, A. 2018 Shear instability of an axisymmetric air—water coaxial jet. J. Fluid Mech. 843, 575–600.
- MOODY, L.F. 1944 Friction factors for pipe flow. Trans. Am. Soc. Mech. Engrs 66 (8), 671-678.
- NÉEL, B., LHUISSIER, H. & VILLERMAUX, E. 2020 'Fines' from the collision of liquid rims. *J. Fluid Mech.* **893**, A16.
- NG, C.L., SANKARAKRISHNAN, R. & SALLAM, K.A. 2008 Bag breakup of nonturbulent liquid jets in crossflow. *Intl J. Multiphase Flow* **34** (3), 241–259.
- NICHOLLS, J.A. & RANGER, A.A. 1969 Aerodynamic shattering of liquid drops. AIAA J. 7 (2), 285-290.
- NIKURADSE, J. 1933 Gesetzmäßigkeiten der turbulenten Strömung in glatten Rohren (Nachtrag). Forschung auf dem Gebiete des Ingenieurwesens 4 (1), 44.
- OSHIMA, I. & SOU, A. 2024 Air-blast atomization of a liquid film. J. Fluid Mech. 985, A36.
- RAYLEIGH, L. 1880 On the stability, or instability, of certain fluid motions. *Proc. Lond. Math. Soc.* 11 (1), 57–72.
- RAYLEIGH, L. 1882 Investigation of the character of the equilibrium of an incompressible heavy fluid of variable density. *Proc. Lond. Math. Soc.* 1 (1), 170–177.
- SCHLICHTING, H. & GERSTEN, K. 2016 Boundary-Layer Theory. Springer.
- SCHNEIDER, C.A., RASBAND, W.S. & ELICEIRI, K.W. 2012 NIH Image to ImageJ: 25 years of image analysis. *Nat. Meth.* 9 (7), 671–675.
- SHINAN, C., WEIDONG, Y., MENGJIE, S., MENGYAO, L. & QIYU, S. 2019 Investigation on wavy characteristics of shear-driven water film using the planar laser induced fluorescence method. *Intl J. Multiphase Flow* 118, 242–253.
- SINGH, G., KOURMATZIS, A., GUTTERIDGE, A. & MASRI, A.R. 2020 Instability growth and fragment formation in air assisted atomization. *J. Fluid Mech.* 892, A29.
- TAYLOR, G.I. 1950 The instability of liquid surfaces when accelerated in a direction perpendicular to their planes. I. Proc. R. Soc. Lond. A 201 (1065), 192–196.
- TAYLOR, N.H. & HEWITT, G.F. 1963 The motion and frequency of large disturbance waves in annular twophase flow of air-water mixtures. *Chem. Engng Sci.* 18 (8), 537–552.
- VARGA, C.M., LASHERAS, J.C. & HOPFINGER, E.J. 2003 Initial breakup of a small-diameter liquid jet by a high-speed gas stream. J. Fluid Mech. 497, 405–434.
- VARKEVISSER, T., KOOIJ, S., VILLERMAUX, E. & BONN, D. 2024 Effect of high wind speeds on droplet formation in sprays. J. Fluid Mech. 1000, A86.
- VILLERMAUX, E. 1998 On the role of viscosity in shear instabilities. Phys. Fluids 10 (2), 368–373.
- VILLERMAUX, E. 2007 Fragmentation. Annu. Rev. Fluid Mech. 39 (1), 419-446.
- VILLERMAUX, E. 2020 Fragmentation versus cohesion. J. Fluid Mech. 898, P1.
- XUE, Y., STEWART, C., KELLY, D., CAMPBELL, D. & GORMLEY, M. 2022 Two-phase annular flow in vertical pipes: a critical review of current research techniques and progress. Water 14 (21), 3496.
- ZANDIAN, A., SIRIGNANO, W.A. & HUSSAIN, F. 2018 Understanding liquid-jet atomization cascades via vortex dynamics. *J. Fluid Mech.* **843**, 293–354.
- ZHANG, P., DI, D., JIN, Y., LI, J., YAN, Y. & TANG, H. 2023 Experimental investigations on dynamic wave structures of a prefilming atomizer. *Phys. Fluids* **35** (6), 065105.
- ZHAO, Y., MARKIDES, C.N., MATAR, O.K. & HEWITT, G.F. 2013 Disturbance wave development in two-phase gas-liquid upwards vertical annular flow. *Intl J. Multiphase Flow* 55, 111–129.